Smoldering Combustion in Oil Shales: Influence of Calcination and Pyrolytic Reactions

Mustafa Elayeb, Gerald Debenest, Valeri V. Mourzenko, Jean-François Thovert

To cite this version:

Mustafa Elayeb, Gerald Debenest, Valeri V. Mourzenko, Jean-François Thovert. Smoldering Combustion in Oil Shales: Influence of Calcination and Pyrolytic Reactions. Transport in Porous Media, 2017, 116 (2), pp.889-921. 10.1007/s11242-016-0805-9 . hal-03109940

HAL Id: hal-03109940
https://hal.science/hal-03109940v1

Submitted on 14 Jan 2021

HAL is a multi-disciplinary open access archive for the deposit and dissemination of scientific research documents, whether they are published or not. The documents may come from teaching and research institutions in France or abroad, or from public or private research centers.

L'archive ouverte pluridisciplinaire **HAL**, est destinée au dépôt et à la diffusion de documents scientifiques de niveau recherche, publiés ou non, émanant des établissements d'enseignement et de recherche français ou étrangers, des laboratoires publics ou privés.

Submitted to Transport in Porous Media, manuscript No.
(will be inserted by the editor)

Smoldering combustion in oil shales. Influence of calcination and pyrolytic reactions.

Mustafa Elayeb · Gérald Debenest · Valeri V. Mourzenko · Jean-François Thovert

Received: date / Accepted: date

Abstract A three-dimensional numerical tool for the microscale simulation of smoldering in fixed beds of solid fuels is presented. The description is based on the local equations and accounts the local couplings of the transport and reaction mechanisms. The chemical model includes devolatilization and cracking of the kerogen, calcination of the carbonates contained in a mineral matrix, and oxidation of the carbon char left by the pyrolysis. An extensive survey of the functioning regimes exhibits features that have to be taken into account in the operation of a reactor and in its macroscopic modeling. Three dimensionless numbers are shown to control the phenomenology, which embody the effects of the constituent properties and of the operating conditions. One of them, $\mathrm{Pe}_{F,s}$, provides an *a priori* criterion for the validity of a local equilibrium hypothesis, and for the applicability of standard homogenized formulations. The numerical observations comply when $\mathrm{Pe}_{F,s}$ is small with the expectations from of a simple homogenized description, including quantitative predictions of the mean temperature profile, of the consumption of the various reactants and of the relative positions of the reaction fronts. Conversely, local equilibrium is not satisfied when $\mathrm{Pe}_{F,s}$ is large and these approaches fail in several respects. The simple upscaled transport equations are unable to predict the evolution of some of the locally average state variable. Furthermore, strong local deviations of the state variables from their local averages, combined with the non linearity of the kinetic laws, cause the overall reaction rates to differ from those deduced from the mean values. Nevertheless, a successful heuristic model for the spread of the hot and potentially reactive region can be stated, which provides an avenue for further studies.

Keywords Smoldering · Oil shale · Combustion · Pyrolysis · Calcination · Microscale simulations

---

Mustafa Elayeb
Misurata University, Faculty of Engineering, ring road 4, P.O.Box 2478 Misurata, Libya

Gérald Debenes
Université de Toulouse, INPT, UPS, IMFT, 31400 Toulouse, France

Valeri V. Mourzenko
Institut P', CNRS, Bâtiment SP2MI, BP 30179, 86962 Futuroscope Cedex, France

Jean-François Thovert
Institut P', CNRS, Bâtiment SP2MI, BP 30179, 86962 Futuroscope Cedex, France E-mail: thovert@ensma.fr

1 Introduction

Filtration combustion appears in many natural or industrial situations, pertaining for instance to fire hazards, chemical reactors or oil recovery by in situ combustion. It is a very complex process, due to the numerous coupled physical and chemical mechanisms involved, to their much different characteristic time scales, and to the geometrical complexity of the host medium on the microscale. The understanding and theoretical modeling are still subject to many open questions. Experimental investigations are impaired by the difficulty and intrusivity of local measurements. Therefore, detailed numerical simulations are the most natural avenue for significant progresses.

Any model of filtration combustion should at least contain governing equations for the gas flow and oxidizer transport, a heat transport equation and a more or less sophisticated model for the chemical reaction kinetics. Obviously, these equations are strongly coupled and non linear. A detailed statement of the problem at the microscale is provided by [1].

Macroscopic governing equations relate fields that represent volume-averaged local quantities [2–4]. They involve effective coefficients that depend on the microstructure and on the flow and reaction regimes. Their determination requires the solution of the full set of microscale equations in a representative sample [5]. In addition, the validity of homogenized equations requires that the physical quantities vary smoothly on the macroscale. This condition is violated when a relatively thin reaction front exists. Finally, homogenized formulations often rely on the hypothesis of local thermodynamic equilibrium. Whether this condition is met or not can be assessed only by examinations on the microscale [6]. Thus, microscale modeling is required to assess under which conditions the usual models are applicable, to evaluate the associated effective coefficients, and possibly to provide phenomenological indications and modeling guidelines for less amenable situations. Such questions have been investigated on the pore scale for athermal reactions [7–9], but the heat release and thermal problem associated with combustion adds a level of complexity.

The three-dimensional microscale numerical model of smoldering in fixed beds developed in earlier works [10, 11] was intended as a general tool to explore by direct simulation the relationships between local mechanisms and global behaviors, in order to help formulating and implementing a sensible macroscopic description. Steps have been taken in this direction [12, 13] with the characterization of the global phenomenology as a function of a small number of dimensionless operating parameters. The present work proceeds along these lines, and introduces additional chemical processes, of practical importance in industrial applications, and especially when burning oil shales, in situ or in surface after mining.

On one hand, the calcination of the carbonates generally contained in a large amount in the shales is very endothermic, and it can influence the whole process by its strong impact on the global heat balance. On the other hand, the collection of the products of devolatilization and cracking of the kerogen is generally the main objective when burning them, and their ignition is to be prevented. Therefore, decarbonation and kerogen pyrolysis are included in the model, in order to provide the phenomenological knowledge and predictive criteria required for the tuning of operating parameters. It is shown in particular that whereas the added processes do not cause or increase thermal disequilibrium, the lack of local equilibrium can strongly influence these reactions, and indirectly the whole process.

This paper is organized into six main sections. The new additions to earlier implementations of the physicochemical and mathematical models are described in Section 2. Section 3 presents a reference solution that provides a framework for the analysis of the numerical results, and introduces a few important quantities and concepts. The general strategy for the extensive set of simulations is described in Section 4. The results are presented and commented in Section 5 for a stratified medium and in Section 6 for a staggered array of cylinders. Finally, a discussion and elements of conclusions are provided in Section 7.

2 Outline of the physicochemical and numerical models

Except for the newly added calcination and pyrolytic processes, the model is described in full details in [10, 11, 14] and only the main features are recalled.

The materials and operating parameters of co-flow smoldering experiments [15–18] are taken as a reference situation. The physicochemical parameters are set according to their actual values, or to their best available estimates (Table 1). Oil shale grains are packed in a vertical column. Air is blown from the top, where ignition is performed. The flow rate can be varied, but the Reynolds number always remains at most of the order of unity. A reaction front propagates downwards. The temperature within the reaction zone rises up to about 1500K (some regimes that yield even larger temperatures could not be investigated due to limitations of the apparatus). Pyrolytic reactions occur downstream of the front; the kerogen decomposes into gaseous compounds that are taken away by the flow and a solid carbon char that later reacts with the oxygen. The endothermic calcination of the carbonates contained in the shale matrix can occur when the temperature reaches about 1000K.

Oil shales were chosen for their interest as a fossil energy resource, and because their mineral matrix (> 80 %) prevents the grain shape and the bed geometry from significantly evolving during the process. The mass loss only results in an increase of the grain microporosity. Only a small vertical shrinkage of the bed ($\approx 3\%$) and no change in the grain size distribution were observed in the experiments [17, 18].

No evidence of a transition to flaming was detected in [17, 18], nor in [19] where smoldering in beds of semicoke prepared by retorting the same oil shale was studied over a wider range of composition. However, this does not preclude the occurrence of flaming in other circumstances. Assessing the range of the operating parameters where flaming can be expected is part of our objectives. Flaming corresponds to the combustion of a gaseous fuel released in the smoldering front, such as CO or products of pyrolysis, triggered when critical conditions in the pore space are met [20, 21]. This requires that flammability and ignition criteria are simultaneously fulfilled for the onset of homogeneous combustion, i.e., coexistence of minimal combustible gas and oxidizer concentrations and temperature at the same position. The simple model for the oxidative reaction described below assumes that if CO is produced, it is oxidized into CO_2 very close to the solid surface. This apparent reaction producing CO_2 on the solid cannot be termed ”flaming”. However, the pyrolytic gases and oxygen can meet and react in some circumstances for which a criterion is identified.

2.1 Chemical model

The chemical model includes a heterogeneous oxidation reaction and two pyrolytic processes within the grains, and can be summarized by

$$C_{(s)} + O_2 \longrightarrow CO_2 + \Delta H_O \tag{1a}$$

$$K_{(s)} + \Delta H_P \longrightarrow C_{(s)} + V \tag{1b}$$

$$CaCO_{3(s)} + \Delta H_C \longrightarrow CaO_{(s)} + CO_2 \tag{1c}$$

This model with oxidation, calcination and pyrolysis is denoted $\{$OCP$\}$in the following, whereas the simpler model of [10–13] which only involves oxidation is called $\{$O$\}$.

Carbon oxidation is described by a ”one-film model” [22], whereby the whole reaction scheme is summarized by the single exothermic heterogeneous reaction (1a) on the grain surface, with ΔH_O=395 kJ/mol. The delay due to the species transfer within the grains can be neglected without strongly affecting the global behavior under conditions discussed in the previous work [11], which basically require that the grain size is at most millimetric. The single-step reaction (1a) lumps the heterogeneous oxidation of C into CO followed by the gas-phase combustion of CO into CO_2 close to the solid surface. The kinetic law for (1a) is assumed to be fast enough so that it is only limited by oxygen supply, when the temperature T exceeds the threshold $T_{r,O}$=300°C. The precise value of $T_{r,O}$ is of little importance since T is actually always far greater in the reaction zone.

Pyrolytic processes which were not considered in the implementation of [10,11] are added here, namely the kerogen devolatilization and cracking (often simply called ”pyrolysis” hereafter) and carbonate calcination. The complex set of mechanisms involved in the cracking is summarized by the single degradation reaction (1b) where K stands for kerogen, ΔH_P is the required heat supply, C is the char residue and V the gaseous products. The mass fractions of about 20% of C and 80% of V measured in [17] are in the usual range for oil shales. The reaction occurs when temperature exceeds a threshold value $T_{r,p}$. Based on the observations of [15], $T_{r,p}$ = 200°C, and the reaction (1b) is nearly athermal ($\Delta H_P \approx 0$). Hence, the reaction rate is limited by the temperature elevation rate. The gaseous products V are not tracked in the simulations.

Part of them can be heavier molecules which are gaseous at $T_{r,p}$ but condensate further downstream where temperature is lower. In the experiments [17,18], the gas flow and smoldering front progression were oriented downwards. The liquid oil seeped without interfering with the smoldering process nor impairing the gas flow, and it was collected at the bottom of the cell. In other situations not considered here, it may be necessary to account for the two-phase flow downstream of the front. A more detailed chemical model should then be used, for instance by distinguishing at least two classes of pyrolytic gases, with different typical molecular weights and thermochemical properties. The initial amount $[K]^{in}$ of kerogen is often set so that the residual char after complete degradation contains $[C]^{in}$ = 9190 moles of C per m^3 of shale. However, other values of the fuel content corresponding to different values of $[C]^{in}$ are also examined in the simulations.

Carbonate calcination corresponds to the endothermic decomposition (1c). The material in the experiments actually contains a mixture of Ca and Mg carbonates, with slightly different values of ΔH_C. For simplicity, the two species are not distinguished here and the mean value ΔH_C = 154 kJ/mol measured in [15] is applied. Effusion of CO_2 is not regarded as limiting, so the reaction rate is also controlled by the heat supply when temperature exceeds the threshold $T_{r,c}$, taken equal to $T_{r,c}$ = 750°C.

2.2 Balance equations

The governing equations for the gas flow, for the oxygen and heat transports, and the approximations applied to make these problems more amenable are only briefly presented since they are fully detailed in [11] for the {O}case. The {OCP}extension only introduces an additional sink term in the heat transport equation in the solid phase, and balance equations for the immobile kerogen, carbon and carbonate species.

The gas flow in the pore space Ω_g is described by Stokes equation,

$$\nabla p = \mu \nabla^2 \boldsymbol{v}, \qquad \nabla \cdot \boldsymbol{v} = 0 \qquad \text{in } \Omega_g \tag{2}$$

Table 1 Physical constants of the solid and gas materials, at room temperature and at 1000K, typical for the reaction zone, and some properties of the oil shale.

Parameter	Unit	T=300K	T=1000K	
				Gas physical properties
ρ_g	kg m^{-3}	1.16	0.348	Density
c_{pg}	J g$^{-1}K^{-1}$	1.01	1.14	Heat capacity
C_g	J m$^{-3}K^{-1}$	1170	397	Volumetric heat capacity
λ_g	W m$^{-1}K^{-1}$	0.026	0.0707	Thermal conductivity
D_{Tg}	mm^2 s^{-1}	22	180	Thermal diffusivity
D_O	mm^2 s^{-1}	20	200	Mass diffusivity (O_2/air)
				Solid physical properties
ρ_s	kg m^{-3}	2700	2700	Density
c_{ps}	J g$^{-1}K^{-1}$	0.84	1.25	Heat capacity
C_s	MJ m$^{-3}K^{-1}$	2.27	3.375	Volumetric heat capacity
λ_s	W m$^{-1}K^{-1}$	0.979	0.979	Thermal conductivity
D_{Ts}	mm^2 s^{-1}	0.29	0.29	Thermal diffusivity
				Shale properties
$[C]^{in}$	mol/m^3	9190	9190	Fixed carbon content
$[C]^{in}\ \Delta H_O$	GJ/m^3	3.63	3.63	Volumetric heat release
$[CaCO_3]^{in}$	mol/m^3	9750	9750	Carbonate content
$[CaCO_3]^{in}\ \Delta H_C$	GJ/m^3	1.50	1.50	Volumetric heat sink
T_{ad}	K		1076	Adiabatic temperature

where $\boldsymbol{v}$, p and μ are the gas velocity, pressure and viscosity. A no-slip condition is applied on the solid surfaces. Inertial effects are negligible in the investigated range of flow rates, and the gas properties and other physicochemical coefficients are taken constant, with values corresponding to the typical front conditions (see Table 1). Note that the change in mass flow rate due to the gas emissions by reactions (1) is not accounted for in the model. The discussion of the possible influence of this simplification is deferred until Section 7.1, in light of concepts and observations that need to be introduced first. The oxidizer is conveyed by the gas, and its concentration $[O_2]$ is governed by a convection-diffusion equation

$$\frac{\partial[O_2]}{\partial t} + \nabla\cdot(\boldsymbol{v}[O_2] - D_O\,\nabla[O_2]) = 0 \qquad \text{in } \Omega_g \tag{3}$$

where D_O is the diffusion coefficient. Finally, two heat transport equations apply in the gas phase Ω_g and in the solid phase Ω_s,

$$C_g\,\frac{\partial T}{\partial t} + \nabla\cdot(C_g\,\boldsymbol{v}T - \lambda_g\,\nabla T) = 0 \qquad \text{in } \Omega_g \tag{4a}$$

$$C_s\,\frac{\partial T}{\partial t} - \lambda_s\,\nabla^2 T = S_r \qquad \text{in } \Omega_s \tag{4b}$$

where C_i is the volumetric heat capacity of phase i, and λ_i its thermal conductivity. The right-hand-side term in (4b) is the heat sink resulting from the pyrolytic reactions.

These transport equations are coupled by the continuity of temperature across the solid surface $\partial\Omega$, and by the source and sink terms associated with the surface reaction (1a). Therefore, flux balances for oxygen and heat at $\partial\Omega$ read

$$-D_O\,\nabla[O_2]\cdot\boldsymbol{n} = S_O\,, \quad (\lambda_s\,\nabla_s T - \lambda_g\,\nabla_g T)\cdot\boldsymbol{n} = S_T \qquad \text{at } \partial\Omega \tag{5}$$

where $\boldsymbol{n}$ is the unit vector normal to $\partial\Omega$ and S_O and $S_T = S_O\Delta H_O$ are the oxygen sink and heat source due to combustion. The general forms of (4b, 5) can be particularized for the kinetics with threshold temperatures assumed in the present implementation. Since the oxidation rate is either negligible or diffusion-limited, the conditions at $\partial\Omega$ read

$$\begin{cases} \text{if } T < T_{r,O} \text{ or } H_C = 0\,, & \nabla[O_2]\cdot\boldsymbol{n} = 0\,, \quad S_O = 0 \\ \text{if } T \geq T_{r,O} \text{ and } H_C = 1\,, & [O_2] = 0\,, \quad S_O = -D_O\,\nabla[O_2]\cdot\boldsymbol{n} \end{cases} \tag{6}$$

where H_C is a Heaviside step function accounting for the fuel exhaustion, on a per grain basis (see eq. 5 and associated discussion in [11]).

Owing to their fast kinetic laws, the cracking and calcination reactions take place in thin fronts in Ω_s at $T = T_{r,p}$ and $T = T_{r,c}$, separating regions where T is too low for the reactions to occur and regions where kerogen or carbonates are exhausted. In the numerical discrete implementation, a volume element τ in the front remains at constant temperature while [K] or [$CaCO_3$] drop to zero. Temperature cannot exceed $T_{r,p}$ (resp. $T_{r,c}$) as long as kerogen (resp. carbonate) is not exhausted. Therefore,

$$\begin{cases} \text{if } T < T_{r,c} \text{ or } H_{Ca} = 0\,, & S_r = 0\,, \quad \frac{\mathrm{d}}{\mathrm{d}t}[CaCO_3] = 0 \\ \text{if } T = T_{r,c} \text{ and } H_{Ca} = 1\,, & \frac{\mathrm{d}}{\mathrm{d}t}[CaCO_3] = \frac{1}{\tau\,\Delta H_C}\int_{\partial\tau} \lambda_s \boldsymbol{n}_{\mathscr{V}}\cdot\nabla T\,\mathrm{d}s \\ \text{if } T > T_{r,c}\,, & S_r = 0\,, \quad [CaCO_3] = 0 \end{cases} \tag{7}$$

where the step function H_{Ca} denotes the presence of remaining $CaCO_3$ at a position in Ω_s. A similar formalism applies for the cracking reaction (1b), but since $\Delta H_P \approx 0$, it results in the instantaneous conversion of K into C + V in a volume element when T reaches $T_{r,p}$.

Note that the problem is nonlinear because of the expressions for the reaction rates in (6,7). This is not a consequence of the simplified form of the kinetic laws. Arrhenius laws also depend nonlinearly on temperature (stiffly, though continuously) and require that a sufficient temperature level is reached for the onset of a reaction. Endothermic reactions are limited by heat supply, but exothermic reactions can give rise to sudden transitions, and in the first place to the ignition/extinction of the smoldering reaction.

2.3 Implementation

The system is completed by macroscopic upstream boundary conditions, i.e., by the entry gas temperature, oxygen content and flow rate. The simulations are started with the whole system at room temperature. Without loss of generality, the temperatures are always given in the following relative to this reference value. After ignition and a transient period, a steady regime establishes where a reaction front progresses with constant velocity. This behavior is observed both experimentally [18] and numerically (*e.g.*, in Fig.2) and its main characteristics can be predicted from global balance arguments (Section 3). We focus the observation on a region around the reacting zone when the steady regime is reached, *i.e.*, far enough from the inlet to be insensitive to the details of the injection. Similarly, the domain of calculation is set long enough to prevent any disturbance from the downstream boundary in the region of interest. The domain of computation is extended by shifting this boundary further downstream whenever gradients of the state variables start to develop at the outlet during the simulations.

The numerical code implements this model in a full 3d, transient formulation. All details regarding the numerical methods can be found in the afore-mentioned references for {O}, where extensive validation tests have also been presented (especially in [10]). The new features in {OCP}require the introduction of new species, with simple balance equations since they are immobile, and a sink term in the heat transport equation which only

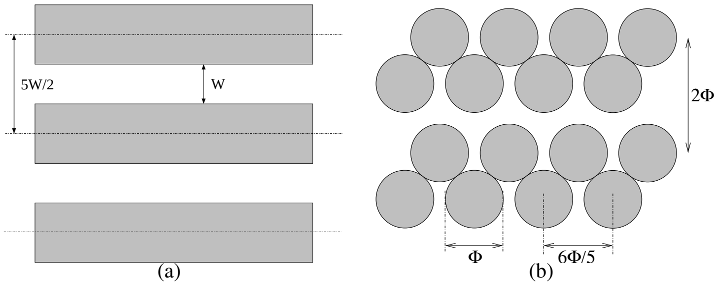

Fig. 1 Two-dimensional geometrical models. Stratified medium with channel aperture W (a) and staggered array with period $L = 6\Phi/5$ of cylinders with diameter Φ (b).

call for minor changes. Let us just mention that a finite volume method is applied for the flow solution [23,24] and for all transfers within the solid, while a random walk approach is applied for the description of all the transports in the gas [25,26]. The heterogeneous chemical reactions are handled by probabilistic production/removal of particles, according to the appropriate kinetic and stoichiometric laws. For performance and stability, the time stepping is adaptive, and in particular, conforms with the changes of regimes in (7) in all the volume elements. The simulations are run in a digital image of the porous medium, made of an array of elementary cubic volume elements.

Although the calculations are actually conducted in 3d, the results in the following correspond to 2d model configurations shown in Fig. 1, a stratified medium and an array of cylinders. Aside from the gain in computational requirements which allows a faster and more exhaustive sweep of the parameters, the main advantage of the 2d models is the possibility of a graphic display for all the local fields, which provides a deeper understanding of the phenomenology than mere average profiles of the same quantities. The whole 2d space is paved with replicas of the patterns in Fig.1, and therefore, periodicity conditions apply for all the variables and fluxes in the direction transverse to the flow and front progression.

3 Reference solution of a homogenized description

A macroscopic point of view is adopted, following for instance [27], in a one-dimensional setting. A steady regime is assumed to be reached. The oxidative reaction front is regarded as vanishingly thin, located at X_F and propagating at velocity U_F. Local thermal equilibrium is assumed here, with a single mean temperature applying both to the gas and solid phases.

3.1 Model $\{O\}$, no pyrolytic reactions

The solid phase initially contains a volumetric amount $[C]^{in}$ of fuel, and the injected gas a concentration $[O_2]^{in}$ of oxygen. After passage of the reaction front, these amounts are reduced to $[C]^{out}$ =$[C]^{in}$ - $\delta[C]$ = ω_C $[C]^{in}$, and $[O_2]^{out}$=$[O_2]^{in}$ - $\delta[O_2]$ = ω_O $[O_2]^{in}$, which are not zero if combustion is incomplete and/or some O_2 escapes. For instance, a fraction $\omega_C \approx 0.12$ of the fixed carbon was found unburned after passage of the front in crushed shales in [17], whereas $\omega_C \approx 0$ applied for a mixture of charcoal with sand in [18]. The front velocity is related to these quantities by a simple stoichiometric balance,

$$U_F = \frac{\varepsilon}{1-\varepsilon}\,\frac{\delta[O_2]}{\delta[C]}\,v^\star \tag{8}$$

where ε is the porosity and $v^\star$ is the mean interstitial gas velocity.

In a referential attached to the front, the heat transport equation reads

$$\widehat{C}\,\frac{\partial T}{\partial t} + \left(\varepsilon\, C_g\, v^\star - \widehat{C}\, U_F\right)\frac{\partial T}{\partial x} - \widehat{\lambda}\,\frac{\partial^2 T}{\partial x^2} = \delta_{X_F} S_H \tag{9}$$

where $\widehat{C} = \varepsilon C_g + (1-\varepsilon) C_s$ is the global volumetric heat capacity and $\widehat{\lambda}$ is a global heat conduction coefficient. The source term S_H, localized at the origin by the Dirac function δ_{X_F} is related to the front velocity, and a temperature T_{ad} can be defined as the ratio of the volumetric heat release and capacity,

$$S_H = (1-\varepsilon)\;\delta[C]\;U_F \Delta H_O\,, \qquad T_{ad} = \frac{S_H}{\widehat{C}\,U_F} \tag{10}$$

Finally, (9) can be written as

$$\frac{\partial T}{\partial t} + (\Delta - 1)\;U_F\,\frac{\partial T}{\partial x} - \widehat{D}\,\frac{\partial^2 T}{\partial x^2} = \delta_{X_F} U_F\; T_{ad} \tag{11}$$

where $\widehat{D} = \widehat{\lambda}/\widehat{C}$ and the dimensionless parameter Δ is given by

$$\Delta = \frac{\varepsilon\, C_g\, v^\star}{\widehat{C}\, U_F} = \frac{(1-\varepsilon)\; C_g}{\widehat{C}}\,\frac{\delta[C]}{\delta[O_2]} \approx \frac{C_g}{C_s}\,\frac{\delta[C]}{\delta[O_2]} \tag{12}$$

Two different stationary regimes can take place, according to the sign of $(1-\Delta)$,

$$\begin{array}{lll} & (x \le 0) & (x \ge 0) \\ \text{if } \Delta > 1: & T(x) = T_p\; \mathrm{e}^{x/\Lambda}\;, & T(x) = T_p \qquad (13a) \\ \text{if } \Delta < 1: & T(x) = T_p\;, & T(x) = T_p\; \mathrm{e}^{-x/\Lambda} \qquad (13b) \end{array}$$

where the decay length Λ and plateau temperature T_p are given by

$$\Lambda = \frac{\widehat{D}}{U_F\,|1-\Delta|}\,, \qquad T_p = \frac{T_{ad}}{|\Delta - 1|} \tag{14}$$

The quantities T_p and Λ involved in the solution (13) are determined by the parameter Δ, which depends on the heat capacities and reactant concentrations, but they are independent of the flow rate. Δ does not depend either on the value of the source term S_H. The unreacted fractions are generally small, *i.e.*, δ[C]$\approx$[C]^{in} and δ[O$_2$]$\approx$[O$_2$]^{in}, and therefore an *a priori* assessment of the main features of the process is possible, in a first approximation and in the framework of this simplified chemical model.

Note that local thermal equilibrium is assumed here, with a same temperature in the solid and gas phases. As shown in the following, this assumption is often invalid in the reaction zone. However, the quantities U_F, S_H, T_{ad} and T_p result from global mass or energy balances and remain unaffected, and (13) still applies far from the reaction front where equilibrium is recovered. This is confirmed by the simulation results, *e.g.* in Fig.6.

3.2 Model {OCP}, including pyrolysis and calcination

The analysis is extended here to account for decarbonation, predict its occurence and the amount of calcinated carbonates. However, most of the results for {O}also apply to {OCP}.

Note first that U_F (8) results from the oxidation stoichiometry and is unaffected by calcination. The parameter Δ (12) is also independent of the occurence of calcination. Consequently, the general form (13) of the temperature profile and the decay length in (14) are also unchanged. Furthermore, these results do not depend on the heat release, except indirectly and marginally through the dependence of the physical coefficients on temperature. They do not depend either on the flow rate, *i.e.*, on Pe, except indirectly for Λ through the hydrodynamic dispersive contribution to $\widehat{\lambda}$, as discussed later (see eq. 24).

However, the adiabatic T_{ad} and plateau T_p temperatures depend on the net heat source S_H, which is modified by the endothermic decarbonation. The net volumetric energy production is the difference between the heat released by carbon oxidation and that consumed by the calcination of a quantity $\delta[\mathrm{CaCO_3}]$ of carbonate. Therefore, S_H and the resulting adiabatic and plateau temperature read

$$S_H = (1-\varepsilon)\ U_F\ \{\delta[C]\ \Delta H_O - \delta[CaCO_3]\ \Delta H_C\} \tag{15a}$$

$$T_{ad} = \frac{\delta[C]\ \Delta H_O - \delta[CaCO_3]\ \Delta H_C}{C_s}, \qquad T_p = \frac{T_{ad}}{|\Delta - 1|} \tag{15b}$$

where ΔH_O and ΔH_C are the heat of the oxidation and calcination reactions. Note that the predictions (15) do not explicitly depend on the flow rate.

It has been assumed in the above that the overall reaction zone is of a small extent compared to Λ, so that all the heats of reaction can be lumped into a single global net value. As shown later, a significant separation of the oxidation and calcination fronts may occur, when T_p widely exceeds $T_{r,c}$. The exponential decay of the temperature profile near X_F is then deformed since the right-hand-side of the heat transport equation (9) actually involves two source/sink terms, in the form of $\delta_{X_{F,O}} S_{H,O} + \delta_{X_{F,C}} S_{H,C}$. However, this does not influence T_{ad} and T_p, since they result from a global thermal balance.

It should be kept in mind that Δ depends (via U_F) on the consumed fractions of C and O_2, and that T_{ad} depends also (via S_H) on the amount of carbonate calcinated into lime. In a wide range of operating parameters, all these species are entirely consumed and the predictions are truly independent of the gas flow rate, but as illustrated later, various mechanisms can cause part of the oxygen to escape the reaction zone, which modifies Δ, the front temperature and possibly the amount of calcinated carbonate. Only the detailed account on the microscale of the complete set of coupled mechanisms can ascertain the actual outcome, but nevertheless, tentative predictions can be formulated. The detailed simulations show that they can provide quite accurate estimations, under conditions related to the flow regime and pertaining to local thermal equilibrium issues.

Consider for illustration the reference situation with the parameters in Table 1. The maximal energy release 3.63 GJ/m^3 for the total carbon oxidation exceeds the maximal sink 1.50 GJ/m^3 required for complete carbonate calcination; therefore, complete calcination is possible. In most cases, the consumed amounts of reactants are equal to their whole initial values. Assume also, subject to *a posteriori* check, that complete calcination is achieved. Equations (12,15) yield Δ=0.384, T_{ad}=631°C and T_p=1024°C (to be compared to T_{ad}=1076°C and T_p=1747°C in the absence of calcination). Thus, T_p is indeed larger than $T_{r,c}$=750°C, which supports *a posteriori* the assumption of complete calcination.

Table 2 Predictions for the adiabatic and plateau temperatures T_{ad} and T_p and for the carbonate calcination rate ω_{ca}, and numerical results of the simulations in stratified media or arrays of cylinders.

			{O}			{OCP}				
Pe	Δ	$\mathrm{Pe}_{F,s}$	T_{ad} (10)	T_p (14)	T_p (Num.)	ω_{ca} (18)	ω_{ca} (Num.)	T_{ad} (15b)	T_p (16)	T_p (Num.)
Stratified medium										
5	0.38	0.71	1076	1747	$\sim$1720	1.00	1.00	631	1024	$\sim$1000
10	0.20	2.71	560	700	$\sim$ 700	0.00	$\sim$0.15	560	700	$\sim$ 640
10	0.28	1.93	784	1088	$\sim$1037	0.54	$\sim$0.51	543	755	$\sim$ 750
10	0.38	1.42	1076	1747	$\sim$1700	1.00	1.00	631	1024	$\sim$1000
10	0.60	0.90	1678	4197	$\geq$4000	1.00	1.00	1236	3089	$\sim$3000
10	1.50	0.36	4197	8394	$\geq$8220	1.00	1.00	3755	7509	$\geq$8000
20	0.18	6.01	504	614	$\sim$ 604	0.00	$\sim$0.09	504	614	$\sim$ 620
20	0.34	3.18	951	1442	$\sim$1411	1.00	1.00	507	768	$\sim$ 780
20	0.38	2.85	1076	1747	$\sim$1700	1.00	1.00	631	1024	$\sim$1000
Array of cylinders										
5	0.38	0.59	1076	1747	$\geq$1550	1.00	1.00	631	1024	$\geq$ 900
10	0.28	1.60	784	1088	-	0.54	$\sim$0.54	543	755	$\sim$ 720
10	0.38	1.18	1076	1747	$\sim$1750	1.00	1.00	631	1024	$\sim$1000
20	0.18	4.97	504	614	-	0.00	$\sim$0.13	504	614	$\sim$ 540
20	0.34	2.63	951	1442	-	1.00	1.00	507	768	$\sim$ 750
20	0.38	2.35	1076	1747	$\sim$1750	1.00	1.00	631	1024	$\sim$1000

More general predictions can be achieved. Suppose for instance that the carbon contents in the shale is changed, still under the assumption of a complete reaction. For low grade fuels with $\Delta < 1$, T_p is related to the fraction ω_{ca} of calcinated carbonates by

$$T_p = \frac{\Delta}{1-\Delta}\,\frac{[O_2]^{in}\Delta H_O}{C_g} - \frac{\omega_{ca}}{1-\Delta}\,\frac{[CaCO_3]^{in}\Delta H_C}{C_s} \tag{16}$$

The fraction ω_{ca} is necessarily 0 when $T_p < T_{r,c}$ and 1 when $T_p > T_{r,c}$, which corresponds to $\Delta < \Delta_0$ and $\Delta > \Delta_1$, respectively, with

$$\Delta_0 = \frac{T_{r,c}}{T_{r,c} + [O_2]^{in}\Delta H_O/C_g}\,, \qquad \Delta_1 = \frac{T_{r,c} + [CaCO_3]^{in}\Delta H_C/C_s}{T_{r,c} + [O_2]^{in}\Delta H_O/C_g} \tag{17}$$

In the intermediate range $\Delta_0 < \Delta < \Delta_1$, $T_p = T_{r,c}$ and partial calcination takes place with ω_{ca} depending on the shale heating value,

$$\omega_{ca} = \frac{\Delta\left(T_{r,c} + [O_2]^{in}\Delta H_O/C_g\right) - T_{r,c}}{[CaCO_3]^{in}\Delta H_C/C_s} \tag{18}$$

For the present values of the parameters, $\Delta_0 = 0.211$, $\Delta_1 = 0.337$, and $\omega_{ca} = 7.98\Delta - 1.69$. The predictions (16,18) are given in Table 2 in comparison with the numerical results in the cases investigated in the simulations.

4 Governing parameters, Regimes, Outline of the simulations

The smoldering process obviously depends on the nature and properties of the reactive solid and of the injected gas. As clearly demonstrated in the previous section, the combination in the dimensionless number Δ of their physicochemical properties is the prominent quantity accounting for them, and it is one of the parameters whose influence is investigated in the simulations. It should be noted that the stated values of Δ are nominal, assuming complete consumption of C and O_2, whereas it turns out sometimes that a significant fraction of oxygen escapes. Hence, its actual value (as well as T_{ad} and T_p) can only be checked *a posteriori*. The nominal Δ is directly related to the shale heating value. Assuming that standard air is injected, that C and O_2 are fully consumed, and C_g and C_s given in Table 1, (12) yields

$$[C]^{in} = 23\,900\Delta \qquad [\mathrm{mol/m^3}] \tag{19}$$

The ratio of organic to mineral matter in most exploitable shales ranges from 0.15 to 0.30 (vs. $\gtrsim$1 for coals) [28], which means that a realistic range for Δ is from 0.2 to 0.5. However, Δ can be decreased by mixing the shale with another inert material, or increased by injecting another gas such as oxygen-depleted air.

The second major operating parameter is the injected gas flow rate, which we quantity by a dimensionless Péclet number,

$$Pe_O = \frac{v^\star \mathscr{L}}{D_O} \tag{20}$$

$\mathscr{L}$ is a characteristic length scale, taken equal to the channel aperture W in the stratified medium and to the grain diameter Φ in the array of cylinders. It compares the characteristic times for oxygen diffusion and convection in the conveying gas. For instance, when Pe_O increases, the oxidizer is carried further away through the medium before it can reach the reactive solid surface by diffusion. Note that Pe_O pertains to the convective-diffusive transport of O_2 in the gas. However, the mass diffusion coefficient D_O and thermal diffusivity $D_{T,g}$ are very similar, which corresponds to the usual situation of a Lewis number Le$\approx$1. Therefore, the thermal Péclet number $\mathrm{Pe}_{T,g}$ based on $D_{T,g}$ is equivalent to Pe_O in the discussion of the functioning regimes, and a single notation Pe is used for both of them henceforth.

Another Péclet number will also be shown to play an important role, namely

$$Pe_{F,s} = \frac{\mathscr{L}\, U_F}{D_{T,s}} = \frac{\varepsilon\, C_g\, D_O}{(1-\varepsilon)\; C_s\, D_{T,s}}\,\frac{Pe}{\Delta} \approx \frac{\varepsilon\, \lambda_g}{(1-\varepsilon)\, \lambda_s}\,\frac{Pe}{\Delta} \tag{21}$$

where the last form assumes that Le $\approx$1. It compares the characteristic times $\mathscr{L}^2/D_{T,s}$ for thermal diffusion in the solid and $\mathscr{L}/U_F$ for the front progression and tells whether the heat produced by the chemical reaction spreads in the solid faster than the front progresses, or whether thermal disequilibrium prevails in the solid in the reaction zone. In the latter case, a mean solid temperature is clearly unrepresentative of the temperature at the reaction site, and its use in the kinetic laws is very questionable. Thus, $\mathrm{Pe}_{F,s}$ provides an a priori criterion for the validity of a local equilibrium hypothesis, and for the applicability of standard homogenized formulations and in particular of the analysis in Section 3. It can also be felt that $\mathrm{Pe}_{F,s}$ determines the width of the hot region around the reaction front and controls the preheating of the solid, with determinant influence on the viability of the smoldering process. Therefore, the expected influence of Δ, Pe and $\mathrm{Pe}_{F,s}$ can be summarized as:

- Δ depends on the system composition and determines the reaction-leading (Δ <1) or trailing (Δ <1) mode, the characteristics of the mean temperature profile (and therefore the positions of the calcination and cracking fronts) and the amount of decarbonation;
- Pe depends on the flow rate, does not give rise to any transition but directly influences the spread of the oxidation reaction zone;

- $\mathrm{Pe}_{F,s}$ depends on both the composition and flow rate, and determines whether local thermodynamic equilibrium can be expected ($\mathrm{Pe}_{F,s} \ll 1$) or not ($\mathrm{Pe}_{F,s} \gg 1$), and in turn whether the predictions in Section 3 for all the major quantities are valid, or if detailed microscale simulations are required.

If confirmed by the simulations, the last item is of the most prominent practical importance.

Extensive simulations presented in Sections 5 and 6 have been conducted to illustrate, confirm and complete these predictions. A reference situation is defined, with the parameters in Table 1 which correspond to Pe=10 and Δ=0.38. Then, other values are examined, by changing the flow rate (*i.e.*, Pe) and the fuel content (*i.e.*, Δ). All other parameters are kept unchanged, which means that $\mathrm{Pe}_{F,s}$ is not independent of Pe and Δ, as shown by (21) which yields $\mathrm{Pe}_{F,s} = 0.0541\ \mathrm{Pe}/\Delta$ in the present case. However, the three numbers are not intrinsically related, since this relation would change if for instance the porosity were modified.

5 Stratified medium

5.1 Influence of the Péclet number Pe

Three cases with Δ=0.38 and Pe=5, 10 and 20 are considered first, *i.e.*, the reference situation and two other cases with air flow rates divided or multiplied by a factor of 2.

5.1.1 Temperature profiles

Longitudinal temperature profiles at successive regularly spaced instants are shown in Fig.2 as functions of the reduced abscissa x/W, where W is the channel width (see Fig. 1a). $\overline{T_s}$ (solid) and $\overline{T_g}$ (gas) are transversely averaged over the corresponding phase. Except for the entry region where cold air is injected, the successive curves differ only by an horizontal shift, which means that a steady regime has established. The expected profiles are obtained, with the plateau temperature $T = T_p$ upstream of the reaction front. The counterparts of Fig. 2 for Pe=5 or 20 (not shown) look exactly the same (recall that both T_p and Λ are independent of Pe). In all cases, with ($\{\mathrm{OCP}\}$) or without ($\{\mathrm{O}\}$) carbonate calcination, the plateau temperatures are in excellent agreement with the prediction (16).

Since a steady regime is reached, the profiles can be considered relative to the oxidation front position X_F and averaged over a relatively long time interval, which reduces the numerical noise. Since the reaction zone is not vanishingly thin, the definition of X_F is partly arbitrary. It is defined here in an average sense as the total current amount of burned carbon divided by the initial carbon content per unit length. Note that X_F progresses at the velocity U_F and that the numerical results comply exactly with the prediction (8) as a consequence of the oxidation stoichiometry. In all situations of reaction-leading mode ($\Delta < 1$), the whole pattern of the reaction zone including the profiles of all the state variables and the positions of the calcination and pyrolysis fronts become stationary relative to X_F.

Figure 3 presents temperature profiles in logarithmic scales, for Pe=5, 10 and 20. Again, the upstream plateau temperatures differ for $\{\mathrm{O}\}$and $\{\mathrm{OCP}\}$, but the exponential decays on the downstream side are identical, as expected in view of (14). The decay rates are also identical for the mean solid and gas temperatures, although the curves can be shifted in the x-direction. However, the decay length Λ is a decreasing function of Pe since U_F et $\widehat{\lambda}$ (which includes a dispersive contribution in the gas) both depend on the flow rate. This dependence is discussed in more details in Section 5.2.

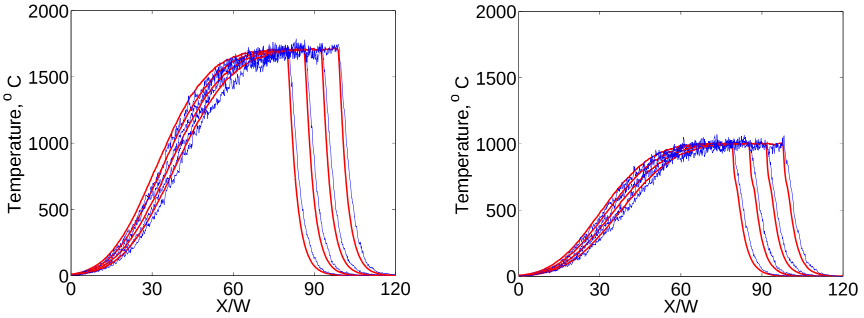

{O} {OCP}

Fig. 2 Longitudinal temperature profiles $\overline{T_s}$ (red) and $\overline{T_g}$ (blue) for {O}and {OCP}at successive regularly spaced times, as functions of the abscissa x/W. Data are for $\Delta = 0.38$ and Pe=10.

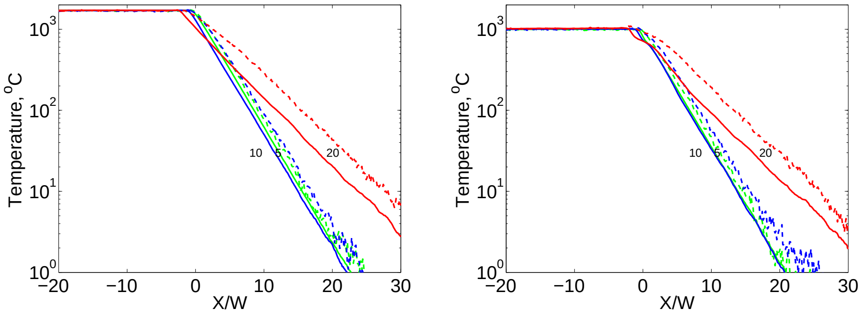

{O} {OCP}

Fig. 3 Temperature profiles $\overline{T_s}$ (——) and $\overline{T_g}$ (− − −) for {O}and {OCP}with $\Delta = 0.38$ and Pe=5, 10 et 20. Distances are measured in channel width W relative to the front position X_F.

Note that if the material contains carbonates, ignoring them in the modeling is not an option. In the example of Fig.2, calcination causes the front temperature to drop by 700°, absorbing more than 40% of the heat released by the combustion. It also produces a lot of CO_2 (more than 2 CO_2 released by burned C). Thus, the question is not whether it is necessary to account for calcination, but rather whether the homogenized model with a lumped reaction in Section 3.2 is sufficient or not for this task. The detailed {OCP}model is applied to explore a range of situations and assess this question.

5.1.2 Concentration profiles

Concentration profiles for the various species are shown in Fig. 4. $[O_2]$ decays exponentially in the reaction zone, with a decay length Λ_O proportional to Pe, as expected since the reaction rate is limited by oxygen supply. A faster flow carries oxygen farther away while it diffuses to the reactive walls. The characteristic time for transverse diffusion is $\tau_O = W^2/\pi^2 D_O$ and oxygen is conveyed at velocity $v_O = (1+3/\pi^2)1.3v^*$ (faster than the mean gas velocity

Table 3 Parameters of the simulations, predicted and numerically observed decay lengths Λ and Λ_O, and fraction ω_O of escaping oxygen.

Stratified medium									
			$\widehat{D}$	Λ/L			Λ_O/L		ω_O
Pe	Δ	$\mathrm{Pe}_{F,s}$	[mm^2]/s	(23)	(26)	(Num.)	(22)	(Num.)	(Num.)
5	0.38	0.71	0.341	2.7	-	3.1	0.82	0.8	0.001
10	0.20	2.71	0.451	0.7	1.9	2.2	1.32	1.4	0.163
10	0.28	1.93	0.451	1.1	2.2	2.5	1.32	1.4	0.069
10	0.38	1.42	0.451	1.8	2.5	3.2	1.32	1.4	0.016
10	0.60	0.90	0.451	4.3	-	5.8	1.32	1.4	0.000
10	1.50	0.36	0.451	8.6	-	9.7	1.32	1.4	0.000
20	0.18	6.01	0.891	0.6	3.7	4.3	2.64	2.7	0.350
20	0.34	3.18	0.891	1.5	4.7	4.9	2.64	2.8	0.077
20	0.38	2.85	0.891	1.8	5.0	5.1	2.64	2.7	0.038
Array of cylinders									
			$\widehat{D}$	Λ/L			Λ_O/L		ω_O
Pe	Δ	$\mathrm{Pe}_{F,s}$	[mm^2]/s	(28)	(29)	(Num.)	(27)	(Num.)	(Num.)
5	0.38	0.59	0.17	1.30	-	1.34	0.21	0.30	0.000
10	0.28	1.60	0.25	0.62	-	0.74	0.42	0.44	0.000
10	0.38	1.18	0.25	0.97	-	1.11	0.42	0.40	0.000
20	0.18	4.97	0.58	0.41	1.02	0.97	0.84	0.87	0.087
20	0.34	2.63	0.58	0.95	1.26	1.35	0.84	0.68	0.000
20	0.38	2.35	0.58	1.13	1.34	1.43	0.84	0.54	0.000

due to its depletion in the low-velocity region near the walls [29]) and therefore,

$$\Lambda_O = v_O \tau_O = \left(1+\frac{3}{\pi^2}\right) v^* \frac{W^2}{\pi^2 D_O}, \qquad \frac{\Lambda_O}{W} = \frac{1}{\pi^2}\left(1+\frac{3}{\pi^2}\right) Pe \approx 0.132 Pe \tag{22}$$

The comparison in Table 3 shows that the numerical observations are in very good agreement with this prediction. In {OCP}, the exponential decay of [O_2] stops at some point and part of the oxygen escapes the reaction zone, about 1.6% when Pe=10 and 3.8% when Pe=20. This occurs when Λ_O is large enough for O_2 to reach the cracking front beyond which fixed carbon has not yet been formed. Since both [O_2] and T are low in this region, oxidative reaction with the kerogen is not expected to be significant and is not included in the model. Basically, oxygen escapes when Λ_O exceeds Λ (see Table 3), as discussed in Section 7.3.

The profiles of carbon and kerogen contents, [C] and [K], show that cracking takes place at a position 4 to 6 W downstream of the oxidation front, dictated by the decay rate of the temperature $\overline{T_s}$, while calcination takes place a short distance downstream of X_F.

5.1.3 Local field maps

The profiles of phase-averaged quantities do not always represent the actual local variables, since strong gradients can exist on the pore scale. This is related to the existence or lack of local thermodynamic equilibrium, and determines the pertinence of locally averaged variables. In the gas, this equilibrium is governed by Pe. It compares the characteristic times for diffusion and convection in the gas, and determines whether the fields can locally equilibrate before convection takes the fluid to another region where the fluid/solid interface conditions are different. The same role is played in the solid by the Péclet number $\mathrm{Pe}_{F,s}$ (21).

Temperature and concentration maps are shown in Fig.5 in a region around the reaction front. The expected effects of the flow rate are observed. The reaction zone, the hot region

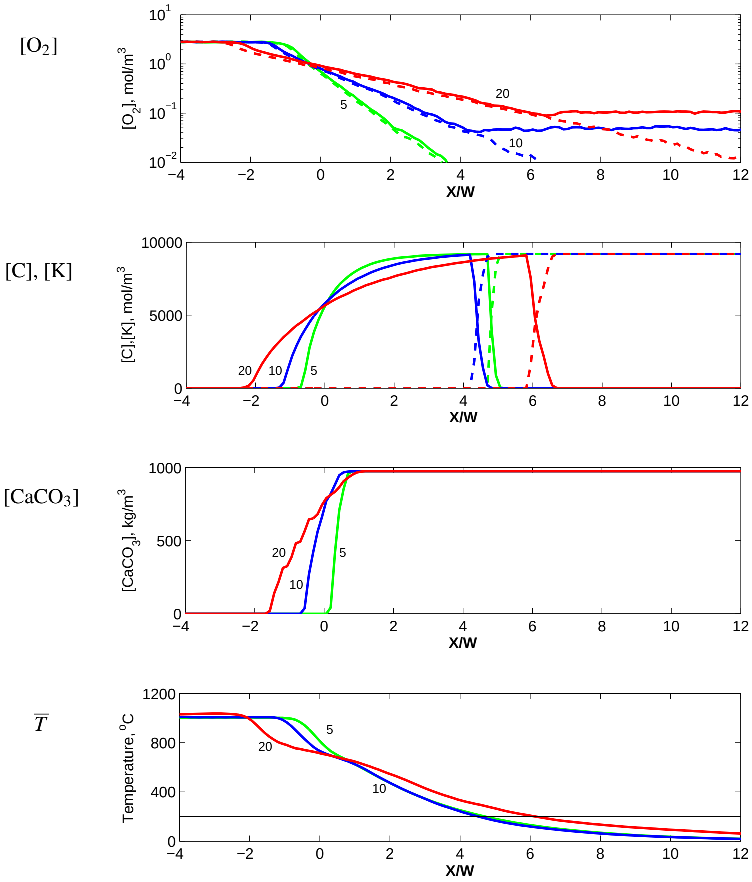

Fig. 4 Profiles of $[O_2]$, of [C] (——) and [K] (– – –), of $[CaCO_3]$ and of $\overline{T_s}$, for {OCP}with $\Delta = 0.38$ and Pe=5, 10 et 20. $[O_2]$ is also shown for {O}(– – –). Distances are measured relative to the front position X_F.

in the gas and the variations of $[O_2]$ and $[CO_2]$ spread over a distance proportional to Pe, as already noted from the mean profiles. Strong concentration gradients exist in the channel, due to the fast oxidation reaction. The transverse thermal gradients in the solid increase with Pe. The isotherms, and in particular those $T_s = T_{r,c}$=750°C and $T = T_{r,p}$ = 200°C which bound the domains where calcination and pyrolysis occur, evolve from nearly orthogonal to the channel axis to very oblique when Pe and $\mathrm{Pe}_{F,s}$ increase, since the front progresses faster while the rate of heat conduction towards the depth of the solid does not change.

5.2 Influence of Δ

The Péclet number is kept constant here (Pe=10 or 20) while Δ varies because of carbon contents $[C]^{in}$ smaller or larger than in the reference case (see eq. 19). $\Delta = 1.5$ with $[C]^{in}$=430 kg/m^3 (larger that the density of most charcoals) is unrealistic for oil shales and it is consid-

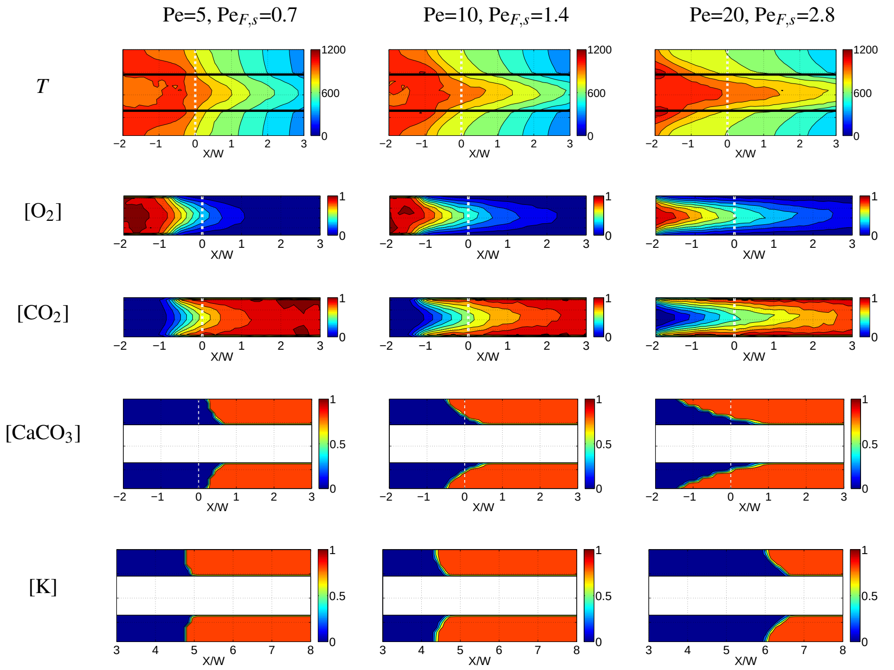

Fig. 5 Maps of the temperature and concentrations [O$_2$]/[O$_2$]^{in}, [CO$_2$]/[O$_2$]^{in}, [CaCO$_3$]/[CaCO$_3$]^{in} and [K]/ [K]^{in} for {OCP}, with $\varDelta = 0.38$ and Pe=5, 10 and 20. Distances are measured in channel width W relative to X_F, indicated by the white vertical broken line. Note that the displayed window is shifted for [K]/ [K]^{in}.

ered only for illustration of general trends. Solid fuels in this range exist, but their characteristics strongly differ from the hypotheses made here of a predominant mineral matrix.

5.2.1 Temperature profiles

Temperature profiles are presented in Fig. 6 for Pe=10 and five values of $\varDelta$. A similar figure for Pe=20 (not shown) can be commented in the exact same way. Again, the upstream plateau and downstream exponential decay are clearly visible when $\varDelta < 1$, with identical decay rates for T_s and T_g. As expected, the situation is reversed for $\varDelta$=1.5. The exponential decay in{OCP}does not start right from the oxidation front but further downstream. $\overline{T_s}$ decreases first nearly linearly between X_F and the calcination front ($T = T_{r,c}$=750°C). This is not in contradiction with the prediction (13), which disregards the details of the mechanisms within the reaction zone (including oxidation and calcination). When this zone is wide, solution (13) applies in the outer regions on either sides.

It is of interest to revisit in details the exponential decay of temperature, and illustrate some of the limitations of an overly simplified macroscopic description.

Assuming local thermal equilibrium, a decay of the temperature beyond X_F (when $\varDelta < 1$) is predicted in the form of (13). By using (8, 20, 12), the decay length can be expressed as

$$\varLambda = \frac{\varDelta}{|1-\varDelta|\ Pe}\ \frac{\widehat{C}}{\varepsilon C_g}\ \frac{\widehat{D}}{D_O}\ W \tag{23}$$

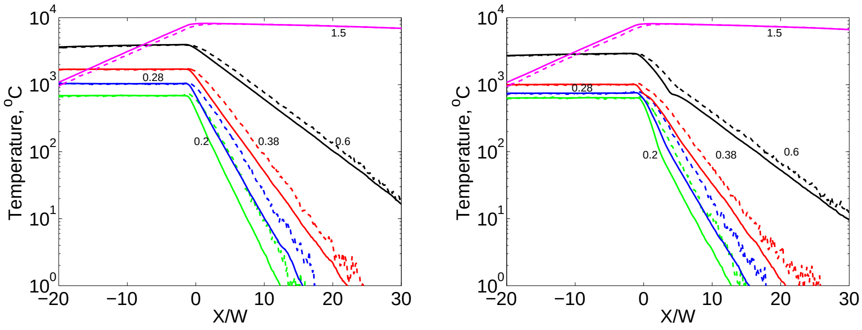

{O}

{OCP}

Fig. 6 Temperature profiles $\overline{T_s}$ (——) and $\overline{T_g}$ (– – –) for {O}and {OCP}with Pe=10 and Δ=0.2, 0.28, 0.38, 0.60 and 1.5. Distances are measured in channel width W relative to the front position X_F.

Λ depends on Δ and Pe, on well known physical coefficients, and on the global, apparent thermal diffusivity $\widehat{D}$, which is more difficult to figure out. It can be evaluated as [12]

$$\widehat{D} = \frac{\widehat{\lambda}}{\widehat{C}} + \frac{\varepsilon C_g}{(1-\varepsilon) C_s}\left[\widetilde{D} + Pe^2_{T,g}\,\mathrm{Da}\right] D_{Tg}\,, \qquad \text{with Da} = \frac{\varepsilon\, C_g\, D_{T,g}}{\Gamma\, W^2} \tag{24}$$

The first two terms correspond to conduction and hydrodynamic dispersion. The last contribution results from the dispersive effect of the coupling of convection with the interphase transfers, with the exchange coefficient Γ upon which the Damkohler number Da is based. Recall that $Pe_{T,g}$ is regarded as equivalent to Pe_O. Furthermore, in a stratified medium, $\widehat{\lambda} = \varepsilon\lambda_g + (1-\varepsilon)\lambda_s$, $\Gamma/\varepsilon C_g = \pi^2 D_{Tg}/W^2 = 1/\tau_O$ [25], and $\widetilde{D} = Pe^2_{T,g}/210$ [30]. This value of $\widetilde{D}$ for passive species and should be corrected when source/sink terms exist along the walls [29], but this is not a serious issue since its contribution to $\widehat{D}$ is small. This yields,

$$\widehat{D} = 0.304\ 10^{-6} + 6.7\ 10^{-11} Pe^2 + 1.4\ 10^{-9} Pe^2 \qquad \mathrm{m^2/s} \tag{25}$$

The success of (23-25) is confirmed by the comparison in Table 3 with Λ determined from the simulation. The agreement is good in the two cases (very different in terms of Pe and Δ) where $\mathrm{Pe}_{F,s}$ is significantly smaller than 1, and reasonable (25% difference) when $\mathrm{Pe}_{F,s}$=0.9.

Conversely, the prediction of (23) is unrealistic when $\mathrm{Pe}_{F,s}$ exceeds 1. This is due to the last contribution in (24, 25). Its evaluation is an asymptotic result reached over a sufficient travel distance, which can exceed the region over which the temperature decays, making the model invalid. Since interphase heat exchanges are the key mechanisms and their characteristic time is related to the front advancement time by $\mathrm{Pe}_{F,s}$, this parameter is indeed expected to determine the validity of (23-25). This illustrates again the key role played by $\mathrm{Pe}_{F,s}$ to characterize the situations where local thermal equilibrium is satisfied, and the validity of predictions based on this hypothesis.

A much better model is provided when $\mathrm{Pe}_{F,s}$ >1 by multiplying (23) by $\mathrm{Pe}_{F,s}$, *i.e.*,

$$\Lambda = \frac{1}{|1-\Delta|}\,\frac{\widehat{D}}{D_{T,s}}\,W\,, \qquad (\ \mathrm{Pe}_{F,s} > 1) \tag{26}$$

This accounts for all the results for $\mathrm{Pe}_{F,s} \geq 1.9$ within at most 14%. However, it must be stressed that (23) and (26) do not have the same status. The former results from the solution of a macroscale equation, within a range of validity. The latter is a heuristic representation of numerical results which applies in another range of non-homogenizable situations, where the lack of local equilibrium prevents locally averaged quantities to be representative. Thus, it is quite remarkable that such a simple and fairly successful model as (26) can be formulated. It is shown in Section 6 that it can be generalized to different kinds of microstructures.

5.2.2 Concentration profiles

Concentration profiles for the various species are given for Pe=10 in Fig. 7. A similar figure for Pe=20 (not shown) gives rise to similar observations. The exponential decay length of $[O_2]$ is identical for all values of Δ, and in good agreement with (22) (see Table 3). As already observed in Fig. 4, this decay is interrupted at the position of the cracking front.

While the positions of the cracking and calcination fronts are not very sensitive to Pe (Fig. 4), they strongly depend on Δ. This results from two combined effects. First, a larger Δ means a larger fuel contents $[\mathrm{C}]^{in}$, which causes T_{ad} and the overall temperature level to increase. Second, Λ increases with Δ, *i.e.*, temperature decays over a larger distance. Both effects contribute to shift in the downstream direction the isotherms $T = T_{r,p}$ and $T = T_{r,c}$. The departure of the calcination front from X_F is the reason for the linear decay of $\overline{T}$ observed in some cases of Fig. 6 before the exponential regime prevails. In the reaction-trailing case of Δ=1.5, the calcination and cracking fronts move away indefinitely downstream of X_F. They do not appear in the interval displayed in Fig. 7 but they are shown in Fig. 8 when $X_F \approx 150W$. Small values of Δ have the opposite effect. The cracking front gets closer to X_F and a notable amount of oxygen escapes in some cases without reacting by lack of fixed carbon, up to about 35% when (Pe=20, Δ=0.18).

Oxidation of the kerogen is unlikely since the temperature decay is also very fast in these cases and $\overline{T_s}$ is very low downstream of the cracking. Thus, the residual oxygen can only react with the gaseous pyrolytic gases, if $\overline{T_g}$ is sufficient for ignition. This cannot be ruled out since $\overline{T_g}$ is significantly larger than $\overline{T_s}$ downstream of X_F, as seen in Figs.6 and 8. This illustrates the potentially detrimental effect of decreasing Δ, which might be desired for other reasons (*e.g.*, reduction of NO_x emission by reduction of the temperature). It brings the cracking front closer to the oxidation front due to the steeper temperature decay, and combustion of the valuable pyrolytic gases is more likely to occur.

Note that the partial escape of O_2 slightly modifies the process parameters. Consider for instance the case of Pe=10, Δ=0.2, with $\delta[O_2]$=0.84 $[\mathrm{O}]^{in}$. The front progression is slowed down, Δ increases which tends to increase T_p. However, a partial calcination (≈15%, see Fig.7) has opposite effects. It decreases the net source S_H, and in turn T_{ad} and T_p. The complete analysis in Section 3.2 accounting for all the combined effects, with $\omega_{ca} = 0.15$ in (16), yields T_p=647°C, in very good agreement with the numerical result (∼640°C).

It may seem paradoxical that even partial calcination takes place while T_p is significantly smaller than $T_{r,c}$.

This results from the lack of local thermal equilibrium and illustrates again the critical role played by $\mathrm{Pe}_{F,s}$. Recall that $\mathrm{Pe}_{F,s}$ = 2.7 when Pe=10, Δ=0.2 (Table 3). The temperature maps in the following show that the local temperature can differ significantly from $\overline{T_s}$ and $\overline{T_g}$ for such values of $\mathrm{Pe}_{F,s}$, and exceed $T_{r,c}$ in part of the solid domain.

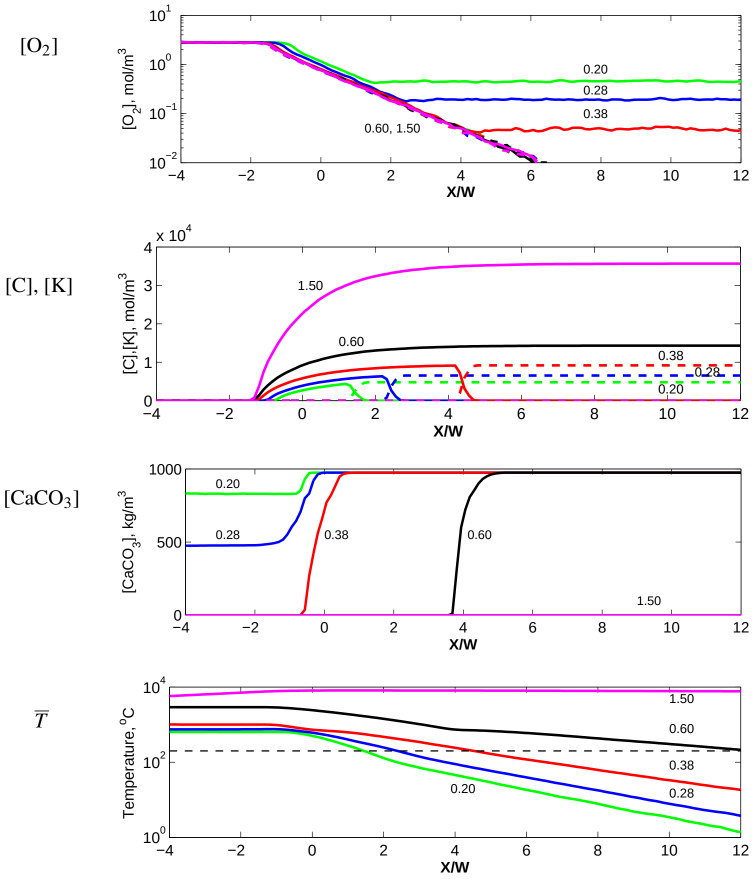

Fig. 7 Profiles of [O$_2$], of [C](——) and [K] (– – –), of [CaCO$_3$] and of $\overline{T_s}$, for {OCP}with Pe=10 and Δ =0.2, 0.28, 0.38, 0.60 and 1.5. The [O$_2$] profiles are also shown for {O}(– – –).

5.2.3 Local field maps

A set of visualizations of the temperature and concentration fields is provided in Fig. 8. [O$_2$] and [CO$_2$] are not displayed since they are always very similar to those for Pe=10 in Fig.5, except for the residual oxygen past the oxidation front when Δ=0.2. The temperature maps clearly show the spread of the hot region when Δ increases. It does not result here from the increase of the reaction zone, as happens when Pe increases, but from the variations of the ratio of the front and heat transport velocities, through the denominator $|1-\Delta|$ in expression (14) for Λ, and from the increase of T_p with Δ. The local homogenization of the temperature when Pe$_{F,s}$ is small (large Δ) is well illustrated in the extreme case of Δ=1.5 (Pe$_{F,s}$ = 0.36).

Complete calcination of the carbonates is observed when $\Delta \geq$0.38, and calcination of about half of it when Δ=0.28, in good agreement with the predictions (16,18) reported in Table 2. However, a thin calcinated layer is also observed for Δ=0.20, despite $T_p < T_{r,c}$. The reason is the heterogeneity of temperature when Pe$_{F,s}$ >1. A hot spot exists in the solid near its surface, on the upstream limit of the oxidation zone. This position has experienced

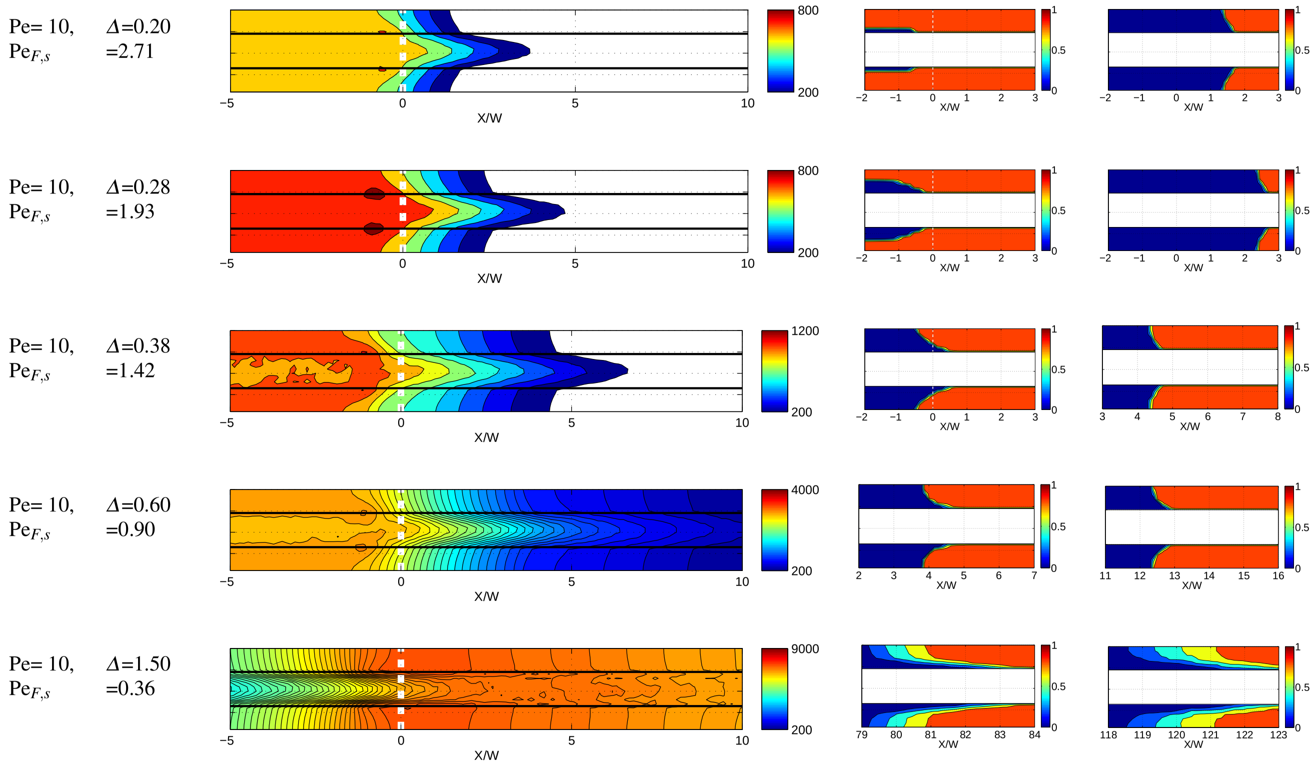

Fig. 8 Maps of the temperature and concentrations $[\mathrm{CaCO_3}]/[\mathrm{CaCO_3}]^{in}$ and $[\mathrm{K}]/[\mathrm{K}]^{in}$ for $\{\mathrm{OCP}\}$, with Pe=10 and Δ=0.20 to 1.50. Distances are measured in channel width W relative to X_F, indicated by the vertical broken lines.

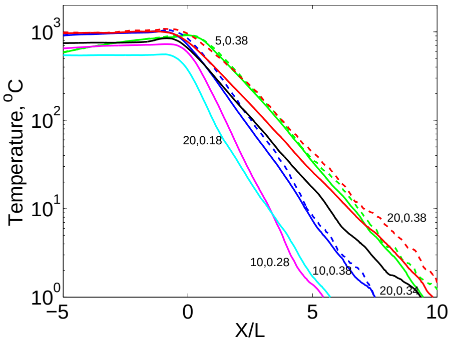

Fig. 9 Temperature profiles $\overline{T_s}$ (solid lines) for {OCP}in the array of cylinders. The labels near the curves give the values of the corresponding parameters (Pe, Δ). Distances are measured in array period L relative to X_F. The gas temperature is also shown for the three cases with Δ=0.38 (broken lines).

complete combustion but the released heat has not been able to spread fast enough in the solid, so that T_s is significantly larger than $\overline{T_s}$ and can exceed $T_{r,c}$. For larger Δ, the calcination front settles further downstream and it moves away indefinitely when $\Delta >1$. The cracking front behaves in a similar way. When $\Delta >1$, it progresses faster than the calcination front. In Fig. 8, both fronts for Δ=1.5 are shown when $X_F \approx 150W$.

Also in the case of Δ=0.2, 16% of the oxygen escapes (Fig. 7), due to the proximity of the isotherms $T_{r,p}$ (cracking front) and $T_{r,O}$ (onset of oxidation), whereas oxygen is carried by the flow further downstream in the middle of the channel. However, due to the large Pe$_{F,s}$ = 2.7, the solid and gas temperatures strongly differ (see Fig. 6b) and T_g exceeds 400°C at the cracking front, where O_2 coexist with the pyrolytic gases. Therefore, ignition of the pyrolytic gases and a transition to flaming are possible.

This is only occurrence of such a risk in the simulations in the layered medium, and it can be predicted from Pe$_{F,s}$ (another occurence appears in similar conditions in the array is cylinders of Section 6) . In all other cases cracking occurs far enough (or T_g decreases fast enough) downstream of X_F for ignition to be prevented. Since on the other hand cracking does not affect significantly the energy balance, its detailed account in the model is not mandatory. Assuming that complete cracking is achieved at a position before the oxidation front reaches it is sufficient. This simplification was used in earlier works with {O}and the present detailed simulations with {OCP}confirm that the assumption was justified.

6 Array of cylinders

The simulations in the array of cylinders described in Fig. 1 have been conducted in the situations listed in Tables 2 and 3. Only those for {OCP}are discussed in details here. Although the effects can be blurred because the length scales and associated time scales in this model are not so clear-cut as in the stratified medium, the same phenomenological features are observed and most of the comments in Section 5 still apply.

Profiles of the mean solid and gas temperatures $\overline{T_s}$ and $\overline{T_g}$ are plotted in Fig. 9 as functions of the position relative to X_F, normalized by the period L of the array. These profiles are moving averages over a $\pm L/2$ interval. Maps of local T fields are shown in Fig. 10. A

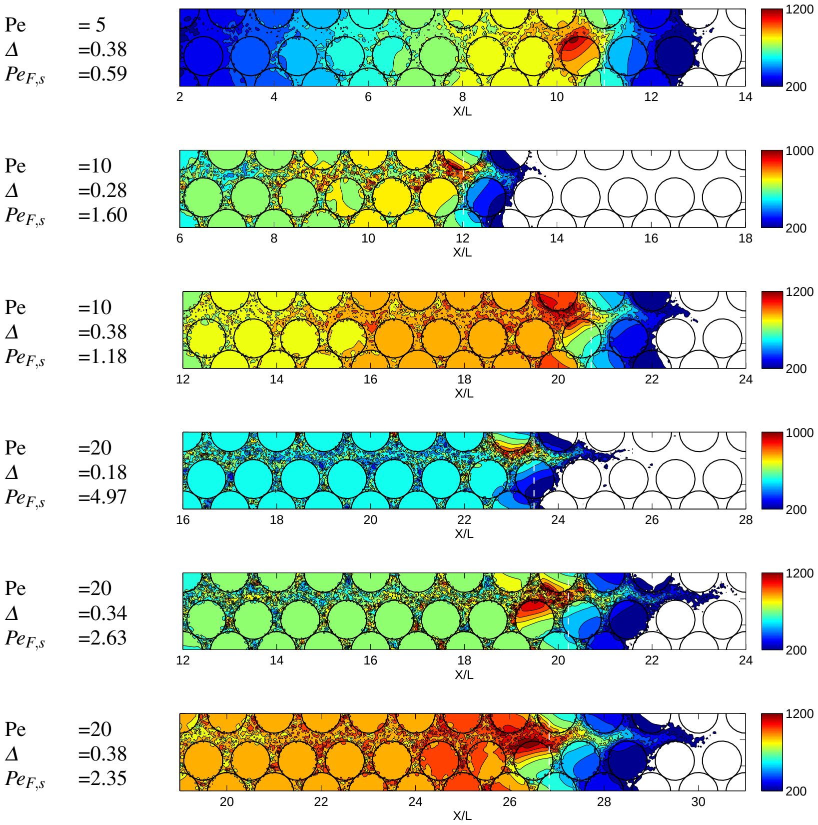

Fig. 10 Temperature fields in the array of cylinders for {OCP}. Distances are measured in periods L of the regular array. The front positions X_F are shown by vertical white broken lines.

very good agreement is observed between the predicted and measured T_p (Table 2), except in two cases. The reason when Pe=5, Δ=0.38 is that the steady regime is not fully established. In the second case (Pe=20, Δ=0.18), it results from the error in the prediction of the calcinated fraction, as discussed below.

The mean temperatures decay exponentially downstream of X_F, as in the stratified medium. The decay lengths Λ/L are listed in Table 3. There is no obvious organization and in particular, Λ/L for the three cases with Δ=0.38 is not a monotonous function of Pe. Still, these results can be rationalized in the framework of a macroscale predictive model, as shown below (see Eqs. 28,29).

The mean profiles in Fig.9 mask a feature which is clearly visible in the maps of Fig.10. A hot spot at the current position of the main oxidation zone is generally present in one of the grain. The same figure a moment later would present a similar spot in the next grain downstream, on the opposite side of the channel. In the case of Pe=20, Δ=0.34, two such spots are visible in Fig. 10 as the picture is taken when oxidation is switching from one grain to the next one. Hence, the stationary pattern of the stratified medium is replaced here by a periodic oscillatory regime. Of course, disordered grain arrangements in a real medium

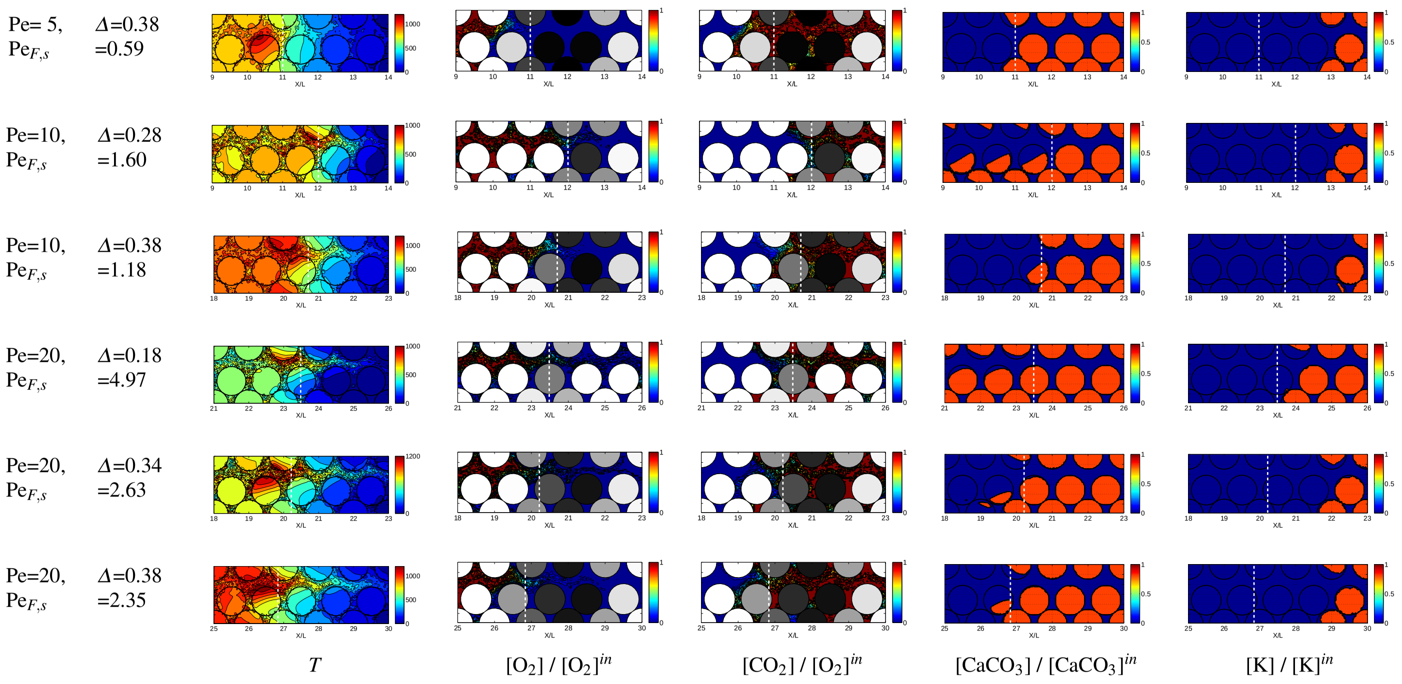

Fig. 11 Maps of the temperature T and concentrations $[O_2]/[O_2]^{in}$, $[CO_2]/[O_2]^{in}$, $[CaCO_3]/[CaCO_3]^{in}$ and $[K]/ [K]^{in}$ for {OCP}in the array of cylinders. Distances are measured in array period L relative to X_F, indicated by the white vertical broken lines. The color of the grains in the $[O_2]$ and $[CO_2]$ maps correspond to the fixed carbon content, from 0 (white) to $[C]^{in}$ (black).

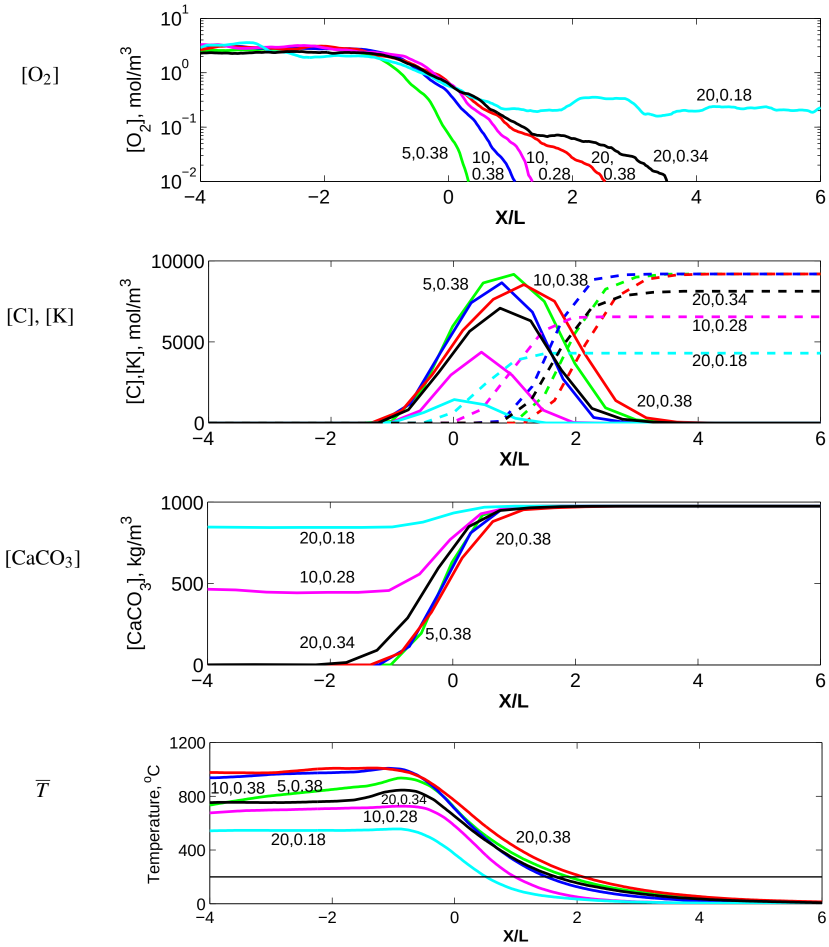

Fig. 12 Profiles of [O$_2$], of [C] (——) and [K] (− − −), of [CaCO$_3$] and of $\overline{T_s}$, for {OCP}with Pe=10 and Δ =0.2, 0.28, 0.38, 0.60 and 1.5, in the array of cylinders. Distances are measured in period L relative to X_F.

would feature the same kind of grain to grain front progression but without the regularity of the present periodic geometric model. The $\pm L/2$ longitudinal moving average roughly correspond to the expected result of an average in a disordered packing along a transverse line crossing randomly positioned grains.

Maps of the temperature and concentrations are provided in Fig. 11, in a $5L$ window around X_F. Profiles of the same quantities averaged transversally and over a moving $\pm L/2$ x-interval are plotted in Fig. 12, as functions of x/L relative to the front position X_F.

Most of the comments made about the stratified medium still apply. The spread of the combustion zone as Pe increases is clearly seen from the O$_2$ concentration profiles in Fig. 12. The decay of $\overline{[O_2]}$ is roughly exponential, with the decay lengths Λ_O/L given in Table 3. Oxygen is fully consumed, except for Pe=20, Δ=0.18 where about 9% escapes. This occurs in the same situation as it did in the stratified medium, for the largest Pe$_{F,s}$ ≈5, due to the same combination of two circumstances: the overall temperature level is low because the fuel contents is small, and oxygen is carried by the gas flow faster than conduction can preheat the solid to ignition temperature (see the discussion in Section 7.3). Since thermal equilibrium is not satisfied, hot gases containing oxygen can reach regions where pyrolysis is underway, and a risk of ignition in the gas exists.

A notable difference of Fig. 12 with Figs.4 and 7 is the longer extent of the pyrolytic reaction zones, which results in part but not only from the $\pm L/2$ moving average. Cracking gave rise in the stratified medium to very sharp variations of [K] et [C], whereas they span here at least a period L. A similar statement applies to calcination. This spread results from the less regular microstructure in the array of cylinders. The unevenness of the geometry and velocity field and the time variations of the general field patterns as the main oxidation zone hops from one grain to another strongly disturbs the shape of the $T_{r,p}$ and $T_{r,c}$ isotherms.

The carbon content is sufficient to give rise to complete calcination of the carbonates in all cases with $\Delta \geq 0.30$, as predicted by (16,18). In the lower grade medium with $\Delta=0.28$, calcination is partial. The observed and predicted values of ω_{ca} are in very good agreement (see Table 2). Finally, no calcination at all is predicted for the leanest fuel with $\Delta=0.18$ but nevertheless, partial calcination with $\omega_{ca} \approx 0.13$ is obtained numerically. This is the same phenomenon as observed in the stratified medium with $\Delta \leq 0.20$, and the reasons are identical. $\mathrm{Pe}_{F,s}$ is very large (≈ 5), and the temperature field is very far from local equilibrium (Fig. 10). Thus, although $\overline{T_s}$ is significantly smaller than $T_{r,c}$, temperature can localy exceed this threshold and allow calcination. As a consequence, the prediction (16) of T_p with $\omega_{ca}=0$ is erroneous, since it overestimates the net heat release. This explains the deviation in Table 2 between the predicted and measured T_p for this case .

Caution is required when applying a homogenized description in cases where local equilibrium is not satisfied, and indeed, discrepancies have been observed in the predictions of Λ in the stratified medium in all cases with $\mathrm{Pe}_{F,s} > 1$. Furthermore, the position of the heat source in the array of cylinders moves in a stepwise way from grain to grain instead of the smooth progression with velocity U_F upon which the definition (21) of $\mathrm{Pe}_{F,s}$ is based. Thus, local equilibrium is not warranted even when $\mathrm{Pe}_{F,s} < 1$. Nevertheless, it is of interest to test whether predictions of the same kind as (22, 23) or (26) have some degree of realism.

Consider first expression (22) for the oxygen concentration decay rate. The mean conveying velocity v_O can be estimated from the volume fractions of the stagnant and actively flowing parts of the pore space (see Fig. 3d of [11]). The former is oxygen-depleted in the reaction area (see Fig. 11) and therefore, v_O is the mean velocity in the latter, *i.e.*, $v_O \approx 2v^*$. The characteristic time τ_O for transverse diffusion can also be estimated by replacing W by a typical pore diameter Φ_p, *i.e.*, $\tau_O = \phi_p^2/\pi^2 D_O$. If Φ_p is taken equal to $\Phi/2$, which is the diameter of the maximal disk that fits in the pore space,

$$\Lambda_O = v_O \tau_O = 2v^* \frac{\Phi^2}{4\pi^2 D_O}\,, \qquad \frac{\Lambda_O}{\mathscr{L}} = \frac{5}{12\pi^2} Pe \approx 0.042 Pe \tag{27}$$

This prediction is in reasonable agreement with the numerical results (Table 3), although Λ_O seems to be slightly less sensitive to Pe than predicted.

The prediction (23) for Λ also applies to the array of cylinders, with W replaced by the grain size Φ, upon which Pe is based,

$$\Lambda = \frac{\Delta}{|1-\Delta| \; Pe} \, \frac{\widehat{C}}{\varepsilon C_g} \, \frac{\widehat{D}}{D_O} \, \Phi \tag{28}$$

and $\widehat{D}$ can be estimated in the same form as (24). The effective conductivity $\widehat{\lambda}$=0.30 W/m.K was calculated by solution of Laplace's equation [31], and $\widetilde{D}$ by the direct solution of the convection-diffusion problem for a passive solute [32]. In the investigated range of Péclet numbers, the results can be represented by $\widetilde{D} \approx 0.071 \;\; \mathrm{Pe}^2$. The definition of Da is also modified by substituting Φ to W, and $\varepsilon C_g/\Gamma$ is still equal to $\tau_O = \phi_p^2/\pi^2 D_O$.

The resulting predictions for $\widehat{D}$ and Λ given in Table 3 can be commented in the same way as for the stratified medium: they are in good agreement with the numerical results when $\mathrm{Pe}_{F,s}$ is small, and strongly underestimate Λ when $\mathrm{Pe}_{F,s}$ is large. But then again, an alternative model of the kind of (26) successfully takes over in the latter case. Note that $\mathrm{Pe}_{F,s}$ is based on the length scale W for the stratified medium. Therefore, its exact counterpart for the array of cylinders should be based on the pore size $\Phi_p = \Phi/2$, whereas it is actually based on the grain size Φ. Alternatively, the discussion can be conducted in terms of $\mathrm{Pe}_{Fs}/2$, which has the same meaning in the cylinders as $\mathrm{Pe}_{F,s}$ in the stratified medium. In view of the data in Table 3, the limit for the validity of (28) appears indeed to be $\mathrm{Pe}_{Fs} \leq 2$ rather than 1. The counterpart of (26) reads

$$\Lambda = \frac{1}{|1-\Delta|} \frac{\widehat{D}}{D_{T,s}} \Phi_p \,, \qquad (\text{when } \mathrm{Pe}_{F,s} > 2) \tag{29}$$

Again, this heuristic model is very successful in the situations of strong local thermal disequilibrium, as shown in Table 3. As a whole, the combination of (27,29) provides good predictions of Λ in the array of cylinders as did their counterparts (22,26) for the stratified medium. In particular, the presence of terms proportional to Pe and to Pe^{-1} in (28), due to the Pe^2 contributions to $\widehat{D}$, explain the non monotonous evolution of Λ with Pe.

7 Discussion

7.1 Influence of the gas emissions

All the reactions in (1) release gases, but the increase of the mass flow rate is not included in the description. This simplification is commented here, and shown not to deprive the model of its predictive capabilities .

The effect of the CO_2 emission from the oxidation reaction (1a) is minor. It does not cause volumetric expansion nor directly influences the velocity field since the number of gas molecules is conserved. Substitution of O_2 by CO_2 increases the density and the mass flow rate, by about 12% if the inlet gas is air, but only slightly modifies the physical properties of the gas mixtures, for instance by -3.9% for the viscosity and -1.5% for the thermal conductivity when T=1000K. However, reactions (1b) and (1c) release larger amounts of matter, corresponding with the present parameters to ≈34% of the mass flow rate of injected air for the cracking, and ≈36% for the calcination of the entire initial carbonate content. This should be taken into account in field scale simulations, since it can influence the overall flow field, including upstream of the reaction zone, and affect the oxygen supply rate. Conversely, this had no effect in the reference experiment [18], due to the finite length and very large permeability of the bed. In any case, the simulations are representative of the process for the specified inlet flow rate, regardless of whether it is imposed (in the experiment) or results (in the field or in a large reactor) from a larger scale flow problem.

Regarding the details of the processes in the reaction zone, no serious perturbation can result from the emission of pyrolytic gases V, since they are always released at its downstream limit. Significant disturbances can only result from the increase of the gas volumetric thermal capacity C_g due to the release of CO_2 by calcination, when it occurs in large amount and close to the oxidation front. This happens in a narrow range of operating parameters, as seen *e.g.* in Fig.7. Calcination is weak for small Δ, and it occurs downstream of the oxidation zone when Δ is large. But when (Pe=10, Δ=0.28), ρ_g and C_g increase by about 30% (including both CO_2 emissions by combustion and calcination). This situation can be predicted from the *a priori* estimates of T_p, Λ and ω_{ca}. Ignoring the gas release does not modify the phenomenology and patterns in the reaction zone, but induces changes that can be quantified. A corrected C_g can be included in the estimation of Δ ($\approx$+30%) and in turn of Λ and T_p (both $\approx$+12%, which tends to shift calcination downstream and minimize the disturbance). U_F and Λ_O are unaffected. Most importantly, the criterion for local equilibrium and applicability of the theoretical predictions is unmodified, since $\mathrm{Pe}_{F,s}$ is independent of the gas properties. Hence, the typology of behaviors observed when using the simplifying approximation is relevant and the reported predictions are quantitatively correct or can in most part be easily corrected.

7.2 Unified expressions for Λ and Λ_O

Many global results such as the predictions of T_p or ω_{ca} have been expressed in a general way as functions of the governing dimensionless parameters, but expressions for some others, namely Λ and Λ_O have been formulated specifically for the two investigated geometrical models. They can easily be reconciled in a tentative general form as follows. Expressions (22, 27) for Λ_O can both be written as

$$\Lambda_O = \eta_O \, \frac{v^* \Phi_p^2}{\pi^2 D_O} \tag{30}$$

where Φ_p is the typical pore diameter and $\eta_O = v_O/v^*$ is equal to 1.3 for the stratified medium and 2 in the array of cylinders. Recall that $\eta_O > 1$ results from the depletion of oxygen in the regions of smallest gas velocity, which correspond to the close vicinity of the solid surfaces in the stratified medium and to vast stagnant dead-end regions in the array of cylinders. These two cases are extreme situations and the associated values are probably practical bounds for η_O. For instance, three-dimensional grain packings are less regular than the stratified medium and contain low- and high-velocity regions, but the flow is nowhere really stagnant.

On the other hand, expressions for Λ (23, 28) when local thermal equilibrium is realized and (26,29) when it is not reduce into

$$\Lambda = \frac{\Delta}{|1-\Delta|\, Pe} \, \frac{\widehat{C}}{\varepsilon C_g} \, \frac{\widehat{D}}{D_O} \, \mathscr{L} \,, \qquad \text{when } \frac{\Phi_p \, U_F}{D_{T,s}} < 1 \tag{31a}$$

$$\Lambda = \frac{1}{|1-\Delta|} \, \frac{\widehat{D}}{D_{T,s}} \, \Phi_p \,, \qquad \text{when } \frac{\Phi_p \, U_F}{D_{T,s}} > 1 \tag{31b}$$

where $\mathscr{L}$ is the arbitrary length scale upon which Pe is based and $\Phi_p \, U_F/D_{T,s}$ is a slightly modified definition of $\mathrm{Pe}_{F,s}$ with $\mathscr{L}$ replaced by Φ_p.

7.3 Roles of the operating dimensionless parameters

The results of the simulations demonstrate the important roles played by the dimensionless parameters Pe, Δ and $\mathrm{Pe}_{F,s}$ in the global behavior of the smoldering process. Since only the flow rate and the solid fuel content have been varied, the three parameters are related in the present simulations, but they are not in a more general framework, as shown by (21).

The parameter Δ which results from the oxygen and fuel contents strongly influences the temperature T_p in the reaction zone and its decay rate away from the front X_F. Reducing Δ when operating a furnace or a large scale reactor, for instance by mixing the reactive material with inert sand, can be viewed as desirable for the purpose of lowering T_p and thereby limiting calcination or NO_x formation and facilitating the reactor design. However, when Δ decreases, the temperature decay is steeper and the cracking front can get very close to the oxidation front, with a risk for the pyrolytic gases and oxygen to encounter and react. This detrimental concomitant effect should be considered in the decision.

The second important operating parameter is the air flow rate, which is the most easily tunable operating parameter. It determines the value of Pe, which does not directly impact the temperature but conditions the reactor fuel combustion and power release rates. But larger flow rates also spread the reaction zone by carrying O_2 faster through the hot reactive region. This can cause part of it to reach a downstream region where the solid is not hot enough to allow carbon oxidation. At best, this oxygen is lost (and the values of U_F, Δ and T_p are modified) and at worst, it can meet the pyrolytic gases in a gas mixture hot enough to allow ignition.

The criterion for oxygen escape is the competition between the decay rates of T and $[O_2]$. If a maximal amount $[O_2]^{out}=\omega_O\ [O_2]^{in}$ of escaping oxygen is targeted, this concentration is reached at $X_F + \ln(\omega_O)\Lambda_O$ whereas the isotherm $T = T_{r,p}$ is located at $X_F + \ln(T_p/T_{r,p})\Lambda$. The former should precede the latter, *i.e.*,

$$\frac{\Lambda_O}{\Lambda} \leq \frac{\ln(T_p/T_{r,p})}{\ln(\omega_O)} \tag{32}$$

This ratio is about 0.4 if a 5% oxygen escape is tolerated. The decay length Λ_O (30) is proportional to Pe. On the other hand, Λ is proportional to $\Delta/(1-\Delta)Pe$ (disregarding the dependence of $\widehat{D}$ on Pe if it is not too large) in view of (31a) for situations of local thermal equilibrium, and to $1/(1-\Delta)$ in view of (31b) in the opposite case. Anyway, the combination of small Δ and large Pe increases the risk of violating (32). This is confirmed by several such instances in Table 3, which are indeed associated with non-zero values of ω_O.

The last parameter $\mathrm{Pe}_{F,s}$ is a criterion for local thermal equilibrium, which is not satisfied when $\mathrm{Pe}_{Fs} > 1$. This makes a straightforward application of a homogenized description problematic, as illustrated for instance by the transition from expression (31a) to (31b) for Λ. It as been shown as well that local deviations from the mean temperature can cause calcination to take place in situations where it is not expected to occur in view of the prediction of T_p, with a significant impact on the net heat balance and thereby on many other aspects of the process.

Note that $\mathrm{Pe}_{F,s}$ scales as Pe/Δ (see Eq. 21) and therefore, the aforementioned combination of small Δ and large Pe corresponds to large values of $\mathrm{Pe}_{F,s}$. Accordingly, situations where oxygen escapes with large values of ω_O are clearly associated in Table 3 with the large values of $\mathrm{Pe}_{F,s}$. Therefore, the heuristic expression (31b) for Λ can be used in practice when checking whether criterion (32) is satisfied.

Finally, the large values of $\mathrm{Pe}_{F,s}$ are associated with the situations of strong thermal disequilibrium, with a high temperature in the gas at a downstream position where oxygen and combustible pyrolytic products coexist. Therefore, the two criteria needed for the onset of flaming are met simultaneously when $\mathrm{Pe}_{F,s}$ is large.

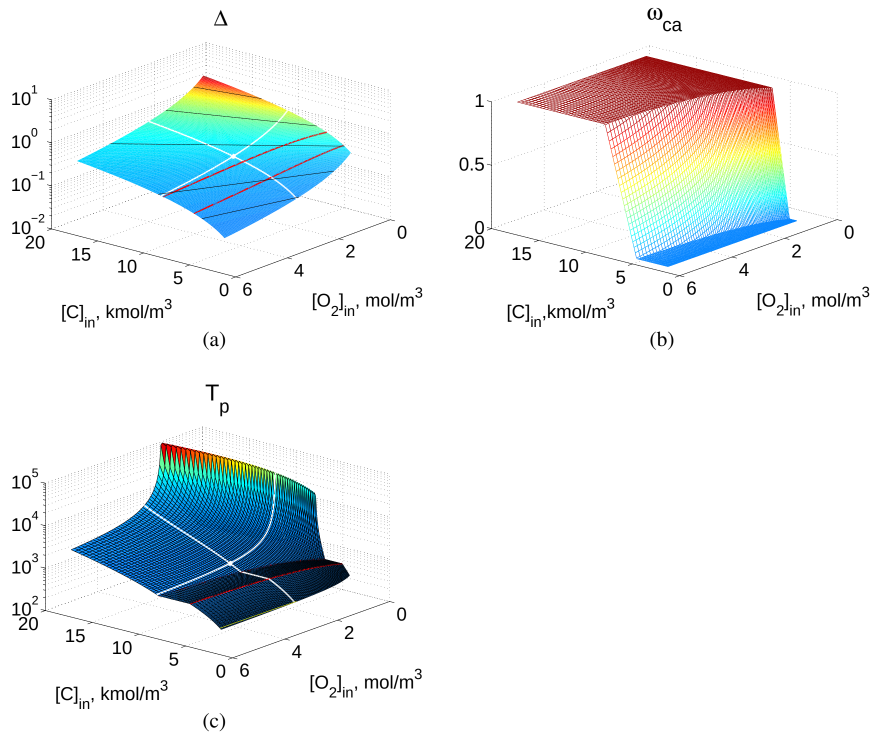

(a)

(b)

(c)

Fig. 13 Parameter Δ and predictions (35, 34) for ω_{ca} and T_p as functions of the fixed carbon and oxygen concentrations. White lines correspond to independent variations of $[\mathrm{C}]^{in}$ and $[\mathrm{O}_2]^{in}$ from the reference case.Red lines bound the domain of partial calcination $0 < \omega_{ca} < 1$.

7.4 Generalized prediction of the calcination rate

An analysis has been presented in Section 3 for the *a priori* estimation of the expected calcination rate ω_{ca} and temperature T_p from global parameters and in particular as a function of Δ. However, different expressions for the criteria (17) prevail if Δ varies because of variations of the fuel contents $[\mathrm{C}]^{in}$ or of the oxidizer inlet concentration $[\mathrm{O}_2]^{in}$. A generalized prediction which explicitly accounts for both of these concentrations is provided here. The adiabatic temperature is related to the calcination rate (to be determined) by,

$$T_{ad} = \frac{[C]^{in}\,\Delta H_O - \omega_{ca}[CaCO_3]^{in}\,\Delta H_C}{C_s} \tag{33}$$

Complete carbon oxidation $\delta[\mathrm{C}]=[\mathrm{C}]^{in}$ is assumed, as observed in practice, as well as $\omega_O \approx 0$ which is satisfied in most cases. Combination of (12,15,33) yields

$$T_p = \frac{[C]^{in}\,\Delta H_O - \omega_{ca}[CaCO_3]^{in}\,\Delta H_C}{C_s[O_2]^{in} - C_g[C]^{in}}\,[O_2]^{in} \tag{34}$$

Thus, if ω_{ca} is stricty comprised between 0 and 1, which implies $T_p = T_{r,c}$, it can be expressed as a function of $[C]^{in}$ and $[O_2]^{in}$

$$\omega_{ca} = \frac{[C]^{in}\ \Delta H_O + C_g[C]^{in}T_{r,c}/[O_2]^{in} - C_sT_{r,c}}{[CaCO_3]^{in}\ \Delta H_C} \tag{35}$$

If (35) yields $\omega_{ca} <0$ or $\omega_{ca} >1$, its actual value is 0 or 1, respectively. In all cases, T_p can be obtained by the value of ω_{ca} in (34). This is illustrated in Fig. 13, for the present physicochemical parameters and carbonate content. Partial calcination occurs in a relatively narrow band and depends primarily on the carbon contents.

7.5 Comparison with experimental data

The carbonate content in the reactive shale and the heat of the calcination reaction have been set in these simulations to the values measured by [16]. The carbon contents are very similar (9190 moles of C per m^3 of shale in the simulations and 8840 in [16]), but the experiments were conducted by mixing 75% of shale with 25% of inert sand. Hence, $[C]^{in}$ is actually 6630 mol/m^3 of solid, and the carbonate content is reduced by the same factor.

Equation (12) yields $\Delta \approx 0.28$, between the two thresholds (17). Therefore, partial calcination is expected, with $\omega_{ca} =0.73$ according to (18). This is in fairly good agreement with the experimental result 0.83. The deviation can be easily explained by differences between the densities and thermal capacities in the model and those of the actual materials. In addition, the relatively narrow domain of partial calcination in Fig. 13 makes the prediction of ω_{ca} very sensitive and the quality of the agreement all the more gratifying.

It is concluded in [16] that with a flow rate corresponding to Pe of the order of unity, the gaseous pyrolytic products escape the reactor without undergoing oxidation. This complies with our observations, even though the real grain packing is much less regular than our model media, both geometrically and compositionally (due to the mixture of reactive and inert grains), and it is probably heterogeneous in some respect. Flow channelization and deformations of the reaction front can take place. This, together with transverse diffusion, might help bring oxygen and pyrolytic gases into contact, but it does not seem to occur in this particular case.

On the other hand, the experimental profiles do not feature the plateau $T = T_{r,c}$ predicted by our model in case of partial calcination. This suggests that the kinetic law adopted here is excessively fast. This is probably true, but the blame on the kinetic model for this discrepancy should be mitigated for several reasons.

For one thing, even though $\mathrm{Pe}_{F,s}$ is small in the experiments, Figs. 10 and 11 show that this does not completely prevent $\overline{T_s}$ and $\overline{T_g}$ from strongly deviating at the front position, and the solid temperature to depart locally from $\overline{T_s}$. This alone was shown to cause partial calcination to occur in situations where none is expected. But it is also difficult to assess exactly in what respect the solid and gas temperature contribute to the response of the thermocouples. The primary product of the fixed carbon oxidation is generally mostly CO, which is later oxidized into CO_2 in the gaseous phase. The two steps are lumped into a single apparent one in the present model, but a more elaborate chemical scheme accounting for them separately shows that CO oxidation can cause the gas temperature to widely exceed that of the neighboring solid [14, 33]. The thermocouples would then record a temperature larger than T_s, which determines the calcination rate and should feature the plateau at $T_{r,c}$. Thus, the numerical and experimental observations are not necessarily in contradiction.

Note also that if the infinitely fast kinetic law for calcination were replaced by a slower one, such as an Arrhenius law, the position of the calcination front would spread and be shifted in the upstream direction, but without affecting the net heat balance and the global behavior, at least as long as transverse heat losses are moderate so that the bed does not cool down fast enough to prevent calcination to occur. Such transverse losses are not taken into account in the numerical model, and it cannot be entirely ruled out that they influence the calcination rate in the combustion cell used in the experiments of [16]. But this artefact would be of much less importance in the practical situations of a wide industrial reactor, or in a transversally unbounded medium for in situ combustion.

7.6 Concluding remarks

The pyrolytic processes of kerogen cracking and carbonate calcination can have a strong and direct impact on the global balances and they can modify the process outcome. An extensive survey of the functioning regimes has exhibited features which can be crucial for the operation of a reactor and for its macroscopic modelisation. Three dimensionless numbers have been shown to control the phenomenology. Their role is summarized in Section 7.3. The parameters Δ and Pe embody the effects of the constituent properties and of the operating conditions (flow rate), respectively, and $\mathrm{Pe}_{F,s}$ depends on both of these aspects. In particular, the latter provides an *a priori* criterion for the validity of a local equilibrium hypothesis, and therefore for the applicability of standard homogenized formulations.

The numerical observations comply when $\mathrm{Pe}_{F,s}$ is small with the expectations from the homogenized description and global arguments presented in Sections 3, 7.2 and 7.4, including quantitative predictions of the mean temperature profile, reactant consumptions and relative positions of the reaction fronts, which determine for instance whether the oxidizer and the valuable pyrolytic gases can meet in conditions where combustion can occur.

Conversely, these approaches fail in several respects when $\mathrm{Pe}_{F,s}$ is large. Firstly, the upscaled transport equations are invalid or for the least, their form or effective coefficients are deeply modified in situations where local equilibrium is not satisfied. Still, a successful heuristic model for the spread of the hot (and potentially reactive) region could be stated. Although not substantiated, this result provides an avenue for further studies into an uncharted domain. Secondly, strong local deviations of the state variables from their averages, combined with the non linearity of the kinetic laws, cause the overall reaction rates to differ from those deduced from the mean values. For instance, calcination can exist when none was expected, with impact on the operating temperature, and possibly in turn on other mechanisms. No suggestion aside from microscale simulation is put forward at this stage to account for the latter effect, but the possibility to identify *a priori* via $\mathrm{Pe}_{F,s}$ the situations at risk requiring a closer examination by a refined homogenized or microscopic approach is valuable.

A microscale description is of course not practicable for simulations in domains covering an oil reservoir or a whole industrial reactor. Achievable grid sizes can at best resolve the reaction region, and at worst exceed the reaction zone thickness, which appears then as a thin surface. If $\mathrm{Pe}_{F,s}$ suggests that local equilibrium can be expected and confidence can be placed in a homogenized model, upscaled equations can be used in the former case and global reaction rates obtained by their integration across the reaction layer thickness can be applied as singular source/sink terms in the latter case. In the opposite situation, a possible approach is the coupling of microscale simulations in an inner, well resolved region covering the smoldering front, with homogenized equations discretized on a coarser grid in the large scale domain upstream and downstream of the front. The implementation and the tuning of such a numerical model are challenging tasks, but the feasibility of the approach was demonstrated by its application (on the downstream side) in [10–13].

Several major extensions to the present model can be contemplated and two have actually been initiated. Radiative heat transfers would regularize the local temperature variations by facilitating heat exchanges between solid bodies, and from hot spots to their surroundings. This issue will be addressed in future works, by the same microscopic approach [34]. A more elaborate chemical model, featuring heterogeneous carbon oxidation into CO followed by CO combustion into CO_2 in the gas phase has also been implemented [14,33]. First applications confirm the major influence on the global behavior of a lack of local equilibrium.

Acknowledgements

This work was supported by the French Research Agency (ANR) through the INSICOMB project (ANR-11-BS09-0005), and by the Erasmus Mundus Al Idrisi II project financed by the Erasmus Mundus Programme of the European Union. It also pertains to the French Government Programme Investissements d'Avenir (LABEX INTERACTIFS, reference ANR-11-LABX-0017-01).

References

1. T.J. Ohlemiller, *Modeling of smoldering combustion propagation*, Prog. Energy Combust. Sci. 11 (1985), pp. 277–310.
2. M.K. Moallemi, H. Zhang and S. Kumer, *Numerical modeling of two-dimensional smoldering processes*, Combust. Flame 95 (1993), pp. 170–182.
3. I.Y. Akkutlu and Y.C. Yortos, *The dynamics of in-situ combustion fronts in porous media*, Combust. Flame 104 (2003), pp. 229–247.
4. I.Y. Akkutlu and Y.C. Yortos, *The Effect of Heterogeneity on In-Situ Combustion: Propagation of Combustion Fronts in Layered Porous Media*, SPE Journal 10 (2005), pp. 394–404.
5. P.M. Adler and J.-F. Thovert, *Real porous media: local geometry and macroscopic properties*, Appl. Mech. Rev. 51 (1998), pp. 537–585.
6. A.A.M. Oliveira and M. Kaviany, *Nonequilibrium in the transport of heat and reactants in combustion in porous media*, Prog. Energy Combust. Sci. 27 (2001), pp. 523–545.
7. A.M. Tartakovsky, G.D. Tartakovsky and T.D. Scheibe, *Effects of incomplete mixing on multicomponent reactive transport*, Adv. Water Resourc. 32 (2009), pp. 1674-1679
8. G. M. Porta, J.-F. Thovert, M. Riva, A. Guadagnini, and P. M. Adler, *Microscale simulation and numerical upscaling of a reactive flow in a plane channel*, Phys. Rev. E 86 (2012) 036102.
9. G.M. Porta, S. Chaynikov, J.-F. Thovert, M. Riva, A. Guadagnini and P.M. Adler, *Numerical investigation of pore and continuum scale formulations of bimolecular reactive transport in porous media*, Adv. Water Resourc. 62 (2013), pp. 243-253.
10. G. Debenest, *Simulation numérique tridimensionnelle, à la microćhelle, de la combustion en lit fixe de schistes bitumineux*, Ph.D. diss., Université de Poitiers, 2003.
11. G. Debenest, V.V. Mourzenko and J.-F. Thovert, *Smoldering in fixed beds of oil shale grains. A three-dimensional microscale numerical model*, Combust. Theory Modelling 9 (2005), pp. 113–135.
12. G. Debenest, V.V. Mourzenko and J.-F. Thovert, *Smoldering in fixed beds of oil shale grains. Governing parameters and global regimes*, Combust. Theory Modelling 9 (2005), pp. 301–321.
13. G. Debenest, V.V. Mourzenko and J.-F. Thovert, *Three-dimensional microscale numerical simulation of smoldering process in heterogeneous porous media*, Combustion Science and Technology 180 (2008), pp. 2170-2185.
14. M. Elayeb, *Modélisation à l'échelle microscopique de transports avec réaction en milieu poreux: Combustion en lit fixe*, Ph.D. diss., Université de Poitiers, Poitiers, 2008.
15. M.F. Martins, S. Salvador, J.M. Commandré, A. Lapene, G. Debenest and J.-F. Thovert, *3D Thermochemical characterization of a combustion front propagation in reactive porous medium: A new experimental device*, Eurotherm Seminar N^o 81, Ecole des Mines d'Albi, France, 2007.

16. M.F. Martins, *Structure dun front de combustion propagé en co-courant dans un lit fixe de schiste bitumineux broyé*, Ph.D. diss., ENSTIMAC, Albi, 2008.
17. M.F. Martins, S. Salvador, J.-F. Thovert and G. Debenest, *Co-current combustion of oil shale - Part 1: Characterization of the solid and gaseous products*, Fuel 89 (2010), pp. 133–143.
18. M.F. Martins, S. Salvador, J.-F. Thovert and G. Debenest, *Co-current combustion of oil shale - Part 2: Structure of the combustion front*, Fuel 89 (2010), pp. 144–151.
19. Sennoune M., S. Salvador and M. Quintard, *Reducing CO2 emissions from oil shale semicoke smoldering combustion by varying the carbonate and fixed carbon contents*, Combust. Flame 158 (2011), pp 2272-2282.
20. Ohlemiller T. J., *Smoldering Combustion*, Section 2, Chapter 9 in SFPE Handbook of Fire Protection Engineering. 3rd Edition 2002, DiNenno, P. J.; Drysdale, D.; Beyler, C. L.; Walton, W. D., Editor(s), 2, 200-210.
21. Rein G., *Smouldering Combustion Phenomena in Science and Technology*, International Review of Chemical Engineering 1 (2009), pp 3-18.
22. S.R. Turns, *An introduction to combustion; Concepts and applications*, McGraw-Hill, N.Y., 1996.
23. R. Lemaître and P.M. Adler, *Transport in fractals. IV-Three dimensional Stokes flow through random media and regular fractals*, Transp. Porous Media 5 (1990), pp. 325-340.
24. D. Coelho, J.-F. Thovert and P.M. Adler, *Geometrical and transport properties of random packings of spheres and aspherical particles*, Phys. Rev. E 55 (1997), pp. 1959-1978.
25. J. Sallés, J.-F. Thovert and P.M. Adler, *Deposition in porous media and clogging*, Chem. Eng. Sci. 48 (1993), pp. 2839–2858.
26. S Békri, J.-F. Thovert and PM.M Adler, *Dissolution of Porous media*, Chem. Eng. Sci. 50 (1995), pp. 2765-2791.
27. D.A. Schult, B.J. Matkowsky, V.A. Volpert and A.C. Fernandez-Pello, *Propagation and extinction of forced opposed flow smolder waves*, Combust. Flame 101 (1995), pp. 471–490.
28. World Energy Council, *Survey of Energy Resources*, ISBN: 0-946121-26-5, World Energy Council, London, 2007.
29. M. Shapiro and H. Brenner, *Dispersion of a chemically reactive solute in a spatially periodeic model of a porous medium*, Chem. Eng. Sci. 43 (1988), pp. 551–571.
30. R. Aris, *On the dispersion of a solute in a fluid flowing through a tube*, Proc. Roy. Soc. Lond. A 235 (1956), pp. 68-77.
31. J.-F. Thovert, F. Wary and P.M. Adler, *Thermal conductivity of random media and regular fractals*, J. Appl. Phys. 68 (1990), pp. 3872–3883.
32. J. Sallés, J.-F. Thovert, R. Delannay, L. Prevors, J.L. Auriault and P.M. Adler, *Taylor dispersion in porous media. Determination of the dispersion tensor*, Phys. Fluids A 5 (1993), pp. 2348–2376.
33. M.E. Elayeb, G.R. Debenest, V.V. Mourzenko and J.-F. Thovert, *3D microscale simulation of smoldering*, Proceedings of the Sixth Mediterranean Combustion Symposium, Ajaccio, Corsica, France, 2009.
34. C. Roudani, *Modélisation à l'échelle microscopique des transferts thermiques radiatifs en milieu poreux*, Ph.D. diss., Université de Poitiers, Poitiers, 2008.